Structures of telomerase at several steps of telomere repeat synthesis

https://doi.org/10.1038/s41586-021-03529-9

Received: 24 November 2020

Accepted: 9 April 2021

Published online: 12 May 2021



Check for updates

Yao He^{1,2}, Yaqiang Wang¹, Baocheng Liu¹, Christina Helmling¹, Lukas Sušac¹, Ryan Cheng¹, Z. Hong Zhou^{2,3 ⋈} & Juli Feigon^{1 ⋈}

Telomerase is unique among the reverse transcriptases in containing a noncoding RNA (known as telomerase RNA (TER)) that includes a short template that is used for the processive synthesis of G-rich telomeric DNA repeats at the 3' ends of most eukaryotic chromosomes¹. Telomerase maintains genomic integrity, and its activity or dysregulation are critical determinants of human longevity, stem cell renewal and cancer progression^{2,3}. Previous cryo-electron microscopy structures have established the general architecture, protein components and stoichiometries of *Tetrahymena* and human telomerase, but our understandings of the details of DNA-protein and RNA-protein interactions and of the mechanisms and recruitment involved remain limited⁴⁻⁶. Here we report cryo-electron microscopy structures of active *Tetrahymena* telomerase with telomeric DNA at different steps of nucleotide addition. Interactions between telomerase reverse transcriptase (TERT), TER and DNA reveal the structural basis of the determination of the 5' and 3' template boundaries, handling of the template-DNA duplex and separation of the product strand during nucleotide addition. The structure and binding interface between TERT and telomerase protein p50 (a homologue of human TPP1^{7,8}) define conserved interactions that are required for telomerase activation and recruitment to telomeres. Telomerase La-related protein p65 remodels several regions of TER, bridging the 5' and 3' ends and the conserved pseudoknot to facilitate assembly of the TERT-TER catalytic core.

Telomerase was first identified in the ciliated protozoan Tetrahymena⁹, which has continued to have a role in the uncovering of the mechanistic details of chromosome end replication^{10,11}. All telomerases contain a catalytic core of TERT and TER, which includes a conserved template and pseudoknot domain (t/PK) and a stem-terminus element¹². Additional TER-binding protein(s) (for example, p65¹³ in *Tetrahymena* and H/ACA small Cajal body ribonucleoprotein¹⁴ in human) are required for TER biogenesis and core ribonucleoprotein assembly. A previous cryo-electron microscopy (cryo-EM) structure of Tetrahymena telomerase at a resolution of 4.8 Å revealed the first complete architecture of TERT⁵: its RNA-binding domain (RBD), reverse transcriptase domain and C-terminal extension (CTE) form a ring structure similar to that of the Tribolium castaneum TERT-like protein¹⁵, whereas the telomerase essential N-terminal domain (TEN) and TRAP motif (Fig. 1a)—which are unique to TERT-cross over the TERT ring from opposite sides to enclose the t/PK and complete the catalytic cavity. Tetrahymena telomerase additionally contains p50 and two replication protein A-related heterotrimeric complexes^{4,10,16}: Teb1-Teb2-Teb3 (TEB) and p75-p45-p19 (Fig. 1a, b). p50, Teb1 and p75-p45-p19 are homologues of human telomere-associated proteins TPP1^{7,8}, POT1¹⁷ and CTC1–STN1–TEN1¹⁸, respectively, which transiently associate with telomerase for telomerase activation, the $handing of single-stranded \, telomeric \, DNA (sstDNA) \, and \, DNA \, polymerase$ α -primase recruitment for complementary strand synthesis¹⁹.

Telomerase repetitively uses its integral template that is complementary to 1.5-1.8 telomere repeats (GGGTTG in Tetrahymena and GGTTAG in human) for several rounds of telomere repeat synthesis¹¹ (Fig. 1c). This requires two types of template translocation: (1) nucleotide translocation that shifts the template by one register after each nucleotide addition and (2) repeat translocation that resets the template back to its original position after synthesis of each telomeric repeat. During repeat translocation, the template must separate from the DNA, shift and then pair to the DNA with its alignment region. To our knowledge, structural details of almost all of these steps are currently lacking. Here we describe the cryo-EM structure at a resolution of 3.3 Å of telomerase with sstDNA at the second step of nucleotide addition, together with structures at the third, fourth and fifth steps. These structures reveal details of protein, RNA and DNA side-chain interactions that determine the assembly, recruitment and activity of telomerase, and suggest a mechanism for processive addition of telomeric repeats.

Overall structure

The endogenously expressed telomerase that we used for our cryo-EM studies was purified from Tetrahymena, and sstDNA (GTTGGG)₅ was added during the purification (Extended Data Fig. 1).

Department of Chemistry and Biochemistry, University of California, Los Angeles, Los Angeles, CA, USA. Department of Microbiology, Immunology, and Molecular Genetics, University of California, Los Angeles, Los Angeles, CA, USA. 3California NanoSystems Institute, University of California, Los Angeles, Los Angeles, CA, USA. 🗵 e-mail: hong.zhou@ucla.edu; feigon@mbi.ucla.edu

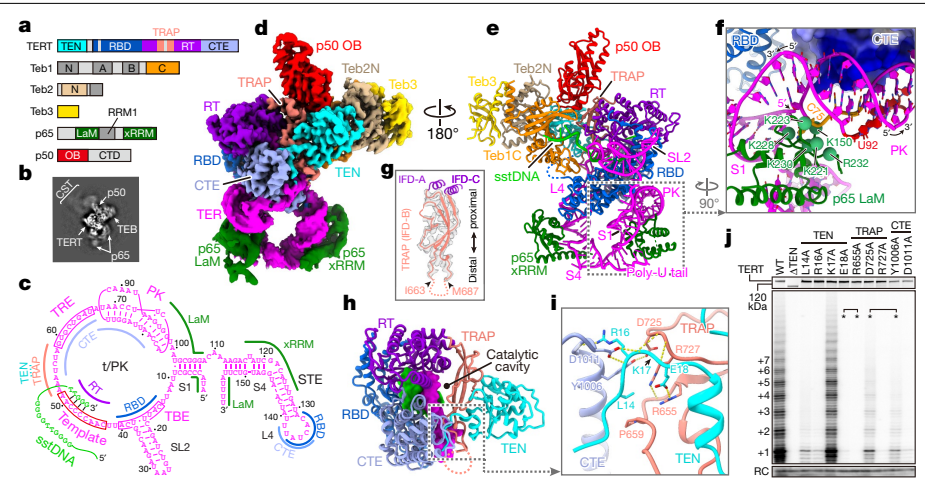


Fig. 1| **Structure of** *Tetrahymena* **telomerase with sstDNA. a**, Domain organization of TERT, p65, p50 and TEB. Regions that are invisible in the cryo-EM map are in grey. CTD, C-terminal domain; LaM, La motif; RT, reverse transcriptase domain. **b**, Representative 2D class average image. CST indicates p75–p45–p19, a homologue of human CTC1–STN1–TEN1. **c**, Schematic of TER secondary structure. Interaction sites with TERT, sstDNA and p65 are indicated. L4, loop 4; PK, pseudoknot; S1, stem1; S4, stem4; SL2, stem-loop 2; STE, stem-terminus element. **d**, Cryo-EM density. **e**, Molecular model of telomerase. **f**, TER pseudoknot and its interactions with the CTE of TERT and La motif of p65. Green spheres are positively charged residues of the La motif of

p65 that are on the interface. The CTE of TERT is shown as electrostatic surface. ${\bf g}$, Superposition of ribbon diagram and cryo-EM density of TRAP. Dashed line indicates TRAP flexible linker. IFD, insertion in fingers domain. ${\bf h}$, Structure of TERT, with DNA (green) and TER (magenta) within the catalytic cavity shown as surfaces. ${\bf i}$, CTE-TRAP-TEN interface. ${\bf j}$, Telomerase activity assays with alanine substitutions of residues shown in ${\bf i}$. Asterisks indicate residues that interact with each other as pairs. The number of telomeric repeats synthesized are indicated at left. Top, expression levels of 35 S-Met-labelled TERT mutants. RC, recovery control. Activity assays were successfully repeated three times. Supplementary Fig. 1 provides gel source data for all figures.

By computationally excluding the dynamic p75-p45-p19 (Fig. 1b), we obtained a reconstruction of sstDNA-bound TERT-TER-p65 core ribonucleoprotein with the p50 oligonucleotide-binding domain (p50 OB) and Teb1C-Teb2N-Teb3 at an average resolution of 3.3 Å (Fig. 1d, e, Extended Data Fig. 2, Extended Data Table 1, Supplementary Video 1).

As was previously seen in a structure at 4.8 Å resolution that used a different sstDNA⁵, the TERT-TER catalytic core adopts an interlocked architecture (Fig. 1e, Extended Data Fig. 3, Supplementary Video 2). In the catalytic cavity, the sstDNA and template form a 4-bp A-form duplex with the final base pair shifted out of the active site (Fig. 1c, h). Almost all of the circle that comprises the t/PK has direct interactions with TERT, including the pseudoknot that is anchored on the CTE by a cluster of positively charged residues (Fig. 1f). The rest of TER, including stem 1 and stem-loop 4, forms a U-shape and is bound by p65 below the TERT ring (Fig. 1e). Loop 4 is inserted between, and specifically interacts with, the RBD and CTE to close the TERT ring (Extended Data Fig. 3d-f).

TEN-TRAP interacts with the TERT ring at only two regions: the N and C termini of TRAP are covalently connected to the insertion in fingers motifs A and C¹², respectively, within the reverse transcriptase domain, and the visible distal end of TRAP is anchored on the CTE together with the N-terminal tail of TEN (Fig. 1g-i, Extended Data Fig. 4a-c). Beyond the distal anchor, TRAP has a 23-residue flexible loop (Fig. 1g); the truncation of this loop has almost no effect on telomerase activity (Extended Data Fig. 4d), consistent with its absence in human TERT (Extended Data Fig. 5a). Behind the anchor, TER runs between and interacts with TRAP and the CTE (Fig. 1h). We investigated the importance of the TEN-TRAP interface and its anchor point on the CTE by assaying the effect of individual amino acid substitutions on telomerase activity. Except for K17A (which has only backbone interactions), all substitutions in the CTE-TRAP-TEN three-way anchor markedly decrease overall activity and repeat addition processivity (RAP) (Fig. 1j, Extended Data Fig. 4f). Substitutions of residues at the extensive (around 1,900 Å²) TEN-TRAP interface generally decrease activity, although less markedly than do substitutions in the anchor (Extended Data Fig. 4e). These results demonstrate that TEN-TRAP and its anchor on the CTE are essential for telomerase activities (including RAP).

p65 binds several regions of TER

p65 is a LARP7 protein²⁰ with a specialized C-terminal RNA recognition motif (xRRM) that bends stem 4 of TER during assembly of the TERT-TER-p65 core ribonucleoprotein^{21,22}, but how the rest of p65 interacts with TER remains uncharacterized. Despite lower resolution in this region, we could model the La motif of p65 with the help of its sequence and structural similarities to human La protein²³. The RRM1 of p65—which completes the La module (La motif–RRM1) (Fig. 1a)—is almost invisible in the cryo-EM map (Fig. 1d), indicating its flexibility. As expected, the La motif of p65 binds the 3'-UUU-OH of TER using a cleft that is lined with conserved aromatic residues²⁰ (Extended Data Fig. 3g). The La motif of p65 also wedges into the junction between the pseudoknot and stem 1 (Fig. 1e,f, Extended Data Fig. 3h). The nucleotide C₇₅ of the pseudoknot loop is flipped out to interact with the positively charged C terminus of the La motif of p65 (Fig. 1f, Extended Data Fig. 3h). The 5' end of TER binds to an adjacent region of the La motif, near the pseudoknot (Extended Data Fig. 3h). Thus, p65 not only bends stem 4 to position loop 4 for interaction with TERT²¹, but its La motif also interacts simultaneously with the 5' end, 3' end and pseudoknot of TER, consistent with a role for p65 as a chaperone for TER folding and ribonucleoprotein assembly.

p50 binds TERT on TEN-TRAP

The role of p50 is functionally equivalent to that of the telomerase-activating role of TPP1 in human 8 . We rebuilt the previous model of p50 OB (amino acids 1–184), and found this domain is highly similar to the TPP1 OB 7 (Fig. 2a, Extended Data Fig. 6a, b). p50 binds TERT at adjacent regions of TEN–TRAP (Fig. 2b). Two structurally conserved loops ($L_{\alpha 2-\beta 4}$ and $L_{\beta 5-\beta 6}$) in the p50 OB bind TEN on a basic surface, and TRAP interacts with the β -barrel and $\alpha 0$ helix of p50 OB (Fig. 2c, Extended Data Fig. 6c). Previous studies have defined the TEL patch and NOB region of human TPP1 OB as critical for telomerase recruitment and RAP stimulation $^{18,24-27}$. Docking TPP1 OB onto our cryo-EM structure reveals that the NOB and TEL patch residues of TPP1 OB are all located on the same interface with TERT as that used by p50 (Fig. 2d,

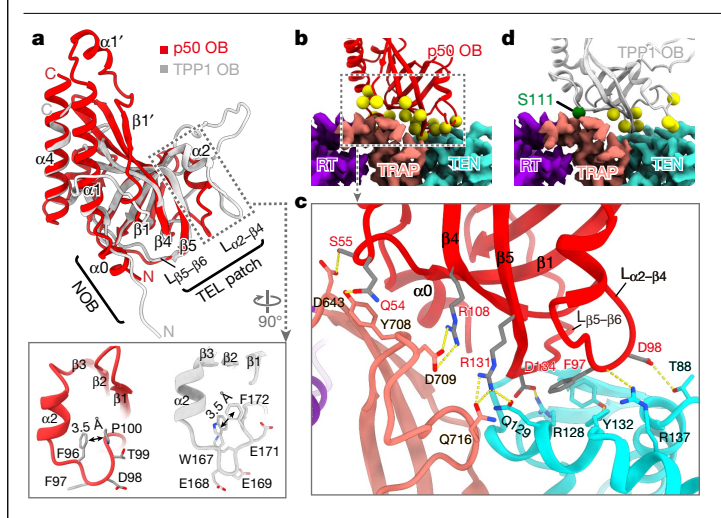


Fig. 2 | **Structure of p50 OB and interactions with TERT. a**, Comparison of p50 OB and human TPP1 OB (Protein Data Bank (PDB) code 2146) structures. Zoomed-in views show $L_{\alpha 2-\beta 4}$ in p50 OB (left) and TPP1 OB (right). **b**, Interface between p50 OB (ribbon, with yellow spheres for residues at interface) and TERT (cryo-EM density). **c**, Side-chain interactions between p50 OB and TENTRAP, as in **b. d**, TPP1 OB docked onto *Tetrahymena* TERT. Yellow spheres are TEL-patch residues. Green sphere is Ser111.

Extended Data Fig. 6d). Residue Ser111, the phosphorylation of which is important for the cell-cycle-regulated TPP1 association with human telomerase 28 , is also located on the interface (Fig. 2d). Notably, the NOB region of TPP1 OB is extended in the crystal structure (Fig. 2a) but—on the basis of sequence similarity (Extended Data Fig. 6d)—probably also forms an $\alpha 0$ when bound to TERT. This structure provides atomic-level details of the TERT–p50 interface, and (by structural homology) for human TERT–TPP1.

Teb1C binds three sstDNA nucleotides

The large subunit Teb1 of TEB handles the sstDNA (similar to human POT1¹⁷), and Teb2 and Teb3 are shared with *Tetrahymena* replication protein A²⁹. Among the four OB-folds of Teb1 (Fig. 1a), Teb1A and Teb1B are known to bind sstDNA with high affinity, but details of the lower-affinity binding mode to Teb1C were unknown³⁰. In our structure, four nucleotides (T_{27} to G_{30}) pair with the template and seven nucleotides $(T_{20} \text{ to } T_{26})$ protrude out of the catalytic cavity and pass near the 5' end of the template (Fig. 3a-c, Extended Data Fig. 6e, f), but do not pair with it (as was previously suggested⁵). We observed continuous sstDNA density from the duplex to Teb1C, which argues against a G-quadruplex in the catalytic cavity or an anchor point on TEN³¹⁻³³. G_{17} , G_{18} and G_{19} are held in the C-shaped oligonucleotide-binding cleft of Teb1C (Fig. 1e, Extended Data Fig. 6e-g) by stacking interactions and three hydrogen bonds to the Watson-Crick edge of G₁₉ (Extended Data Fig. 6h). Alanine substitutions of Phe603 that stacks on G₁₇ and of Lys660 that hydrogen bonds to G₁₉ show substantial defects in sstDNA binding and stimulation of telomerase activity³⁰. The 16 remaining sstDNA nucleotides (G₁ to G₁₆), which are expected to interact with Teb1A and Teb1B, are invisible in the cryo-EM map.

Stabilization of the template-DNA duplex

In our structure, the template +3 nucleotide (C_{46}) is at the active site ready for an incoming dGTP and the final base pair of the duplex is at position +2 (C_{47}); hereafter, we designate this structure as 'telomerase T3D2', in which T3 is the template position and D2 is the duplex position (Fig. 3a–d). Starting from the active site, eight TER nucleotides stack continuously in an A-form conformation (Fig. 3d, Extended Data Fig. 3k). Template

nucleotides that are downstream of the active site (C_{43} to A_{45}) are rotated about 180° away from the duplex and stack together out of the catalytic cavity (Fig. 3d, e). Below the duplex, the unpaired DNA nucleotides are rotated outward by around 120° in a helical stack (Fig. 3d, f). The duplex and adjacent nucleotides are handled by TERT through structural elements that are common to most polymerases (palm, fingers, primer grip, thumb helix (TH) and thumb loop (TL))³⁴, as well as through motifs that are specific to a subset of reverse transcriptases (motif 3³⁵ and T³⁶) or TERT (CP2 (known as TFLY in human)^{37–39} and TRAP⁵) (Fig. 3b–d, Extended Data Fig. 5). Specifically, motif 3 interacts with the template (Extended Data Fig. 3j), TL interacts with the DNA backbone, and TH contacts DNA and TER nucleotides that are 3′ of the template (Fig. 3f).

A newly identified motif in the RBD (which we name the bridge loop (amino acids 411–418)) is spatially located between CP2 and TL, and inserts its conserved tip residues (Arg413 and Phe414) into the major groove of the duplex (Fig. 3h), thereby bridging both ends of the duplex (Fig. 3b-d). On the DNA side, Phe414 breaks the duplex by stacking with T₂₆, and the backbone turn is further stabilized by Lys919 in the TH and Asn904 in the TL (Fig. 3f). Alanine substitution of Phe414 markedly decreases activity and abolishes RAP, whereas the substitutions F414Y and F414H have relatively small effects (Fig. 3g, Extended Data Fig. 4g)—consistent with a requirement for aromatic stacking interactions. On the RNA side, Arg413 contributes to a network of interactions among conserved CP2 (Tyr231), T motif (Glu480) and fingers (Arg534) residues that position the template nucleotide that is downstream of the active site (A_{45}) and flip in the template nucleotide that is opposite the active site (C_{46}) during nucleotide translocation (Fig. 3e). Individual alanine substitution of these residues all decrease activity to less than 20%, and decrease RAP to less than 60% for R413A and E480A and to undetectable levels for R534A and Y231A (Fig. 3g, Extended Data Fig. 4g). The locations of these bridge loop and other residues at either end of the duplex, their sequence conservation, and effects of substitutions on telomerase activity suggest they have essential roles in template guidance and duplex stabilization.

Template-DNA duplex length and handling

We next obtained telomerase structures with the template at position +5 (telomerase T5D5) at a resolution of 3.8 Å, and at position +4 (telomerase T4D4) at a resolution of 4.4 Å (Extended Data Fig. 7), and also refined the duplex model in the previously published 4.8 Å-resolution structure (telomerase T3D3)⁵. By using native sstDNA (for telomerase T3D2) and sstDNA containing locked nucleic acids⁴⁰ (for telomerase T3D3, T4D4 and T5D5), we could trap the duplex in the post- and pre-nucleotide translocation states, respectively (Extended Data Fig. 8). There is little conformational change in TERT between these two states, as has also previously been observed for *Tribolium* TERT-like protein⁴¹.

Comparison of these structures reveals an identical conformation of RNA nucleotides within the catalytic cavity (Fig. 3d, Extended Data Fig. 8). At each step, as the template–DNA duplex moves, the downstream template nucleotide flips into the active site and the previously stacked 3′ nucleotide flips out, maintaining a total of eight nucleotides in the stack. Concurrently, the sstDNA interacts with the template to form a 4- or 5-bp duplex, depending on whether it is in the post- or pre-nucleotide translocation state, respectively. For each register of the duplex, interactions with the bridge loop, TH and TL are maintained (Extended Data Fig. 8). These structures provide direct evidence for template–DNA duplex length and handling at different steps of telomere repeat synthesis, and suggest that only four stable (post-nucleotide translocation) base pairs—stabilized by the unique bridge loop of telomerase—are present at each step.

Template boundaries and movement

The 5' and 3' template boundaries are determined by TERT interactions with the template boundary element (TBE)⁴² and template recognition

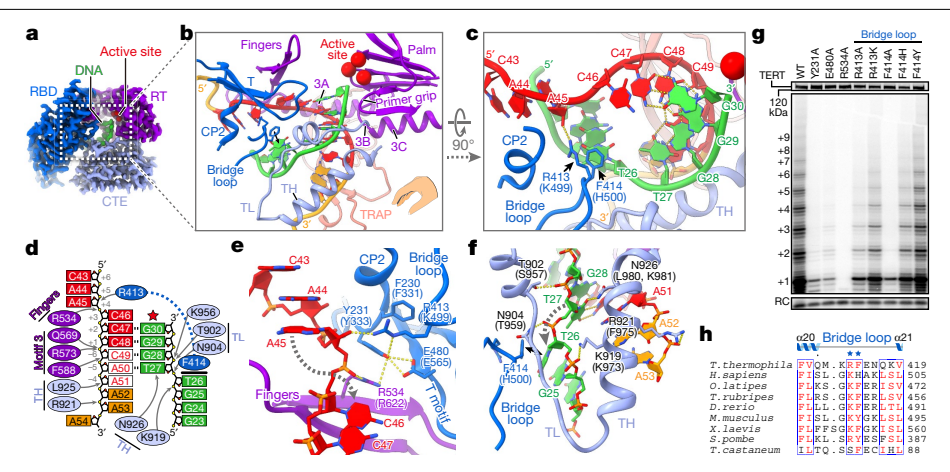


Fig. 3 | Interactions between TERT and template-DNA duplex. a, Cryo-EM densities of TERT and template-DNA. Red spheres are active-site residues (Asp618, Asp815 and Asp816). b, c, Ribbon depictions of template-DNA and TERT motifs involved in duplex handling. Template and adjacent nucleotides are red and orange, respectively. Bridge loop Arg413 and Phe414 are shown as sticks. The hand (inset in b) shows orientation relative to other polymerases. d, Schematic showing specific interactions between TERT and template-DNA.

Template alignment nucleotides are red with a white background. Arrows indicate sites of polar interactions. Bold line indicates Phe414 and T₂₆ stacking interaction. e, f, Side-chain interactions surrounding the template (e) and DNA (f) nucleotide flipping regions. The corresponding human TERT residues are in parentheses. g, Telomerase activity assays with TERT substitutions on CP2, T motif, fingers and bridge loop. n = 3 independent experiments. **h**, Sequence alignment of the bridge loop, with conserved residues in red.

element (TRE)⁴³, which are connected to the template by linkers that are denoted TBE_L and TRE_L⁵, respectively (Fig. 4a). Comparison of the other structures with T3D2 reveals that the TBE and TRE remain fixed on TERT as the template moves from the +3 to +5 position (Fig. 4a-e, Extended Data Fig. 9a-c). On the 5' side of the template, the TBE is anchored on RBD by CP2, CP and T motifs 37 , plus additional stacking and hydrogen-bonding interactions for C_{39} and A_{40} at the 3' end of the TBE $(Fig.\,4d, Extended\,Data\,Figs.\,3c, 9b).\,On\,the\,3'\,side\,of\,the\,template, the$ TRE $(G_{59} \text{ to } U_{66})$ wraps along—and has numerous stacking interactions with—a stripe of five aromatic residues on the CTE (Fig. 4e, Extended Data Fig. 9c). The TRE backbone adopts a compressed zigzag conformation with a $U_{60} \cdot U_{63}$ base pair in the middle.

Unlike the fixed TBE and TRE, TBE₁ (U_{41} and U_{42}) and TRE₁ (A_{52} to A_{58}) exhibit conformational changes that are consistent with concerted stretching and looping⁴⁴ as the template moves through the active site (Fig. 4b, c). In telomerase T3D2, the TBE₁ and +4,+5 and +6 template nucleotides are looped out, with U₄₁ and U₄₂ pointing outward in opposite directions (Fig. 4d). However, in telomerase T5D5 (in which only the +6 template nucleotide is out of the catalytic cavity), the backbone of TBE₁ is more stretched (Fig. 4c, Extended Data Fig. 9b). Basic residues (Arg550, Lys551 and Lys553) that are located on an extended finger-shaped linker between motif 2 and motif 3A (amino acids 550-560, which we name motif 3N) provide a surface for TBE₁ to slide over (Fig. 4d, Extended Data Fig. 3a). Individual alanine substitutions of these residues decrease telomerase activity to less than 40% and deletion of motif 3N abolishes activity (Fig. 4i), confirming the importance of the interaction between motif 3N and the TBE₁.

On the 3' end of the template, TER passes through a positively charged, hourglass-shaped channel formed by TH and TRAP (Fig. 4f). The upper part of the channel is lined by basic residues (Lys657, Arg658

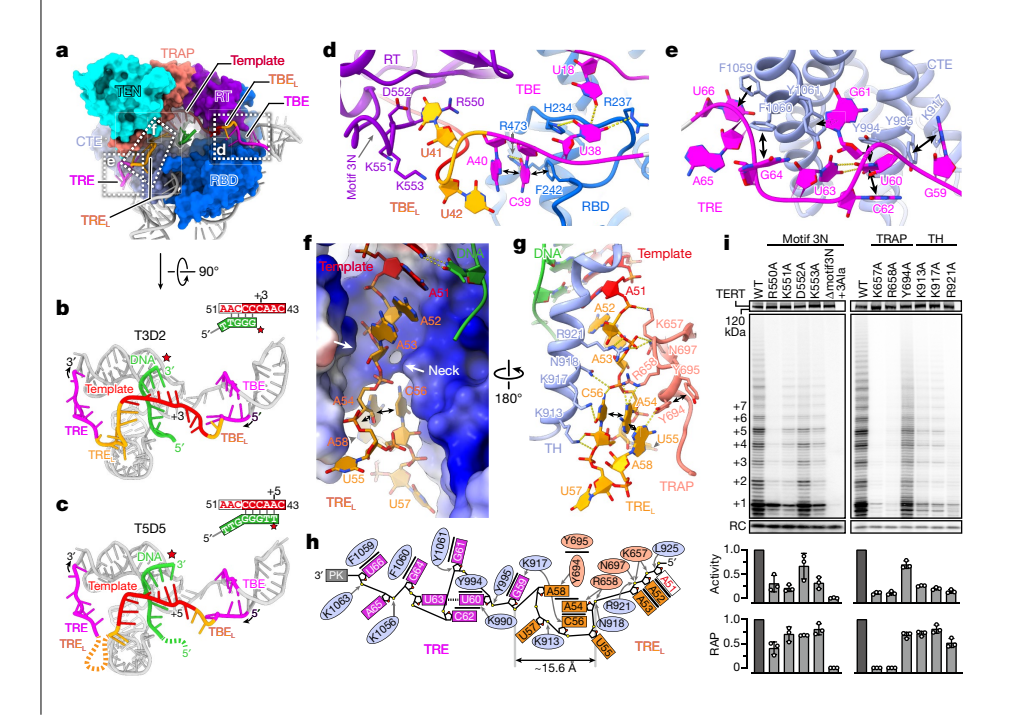
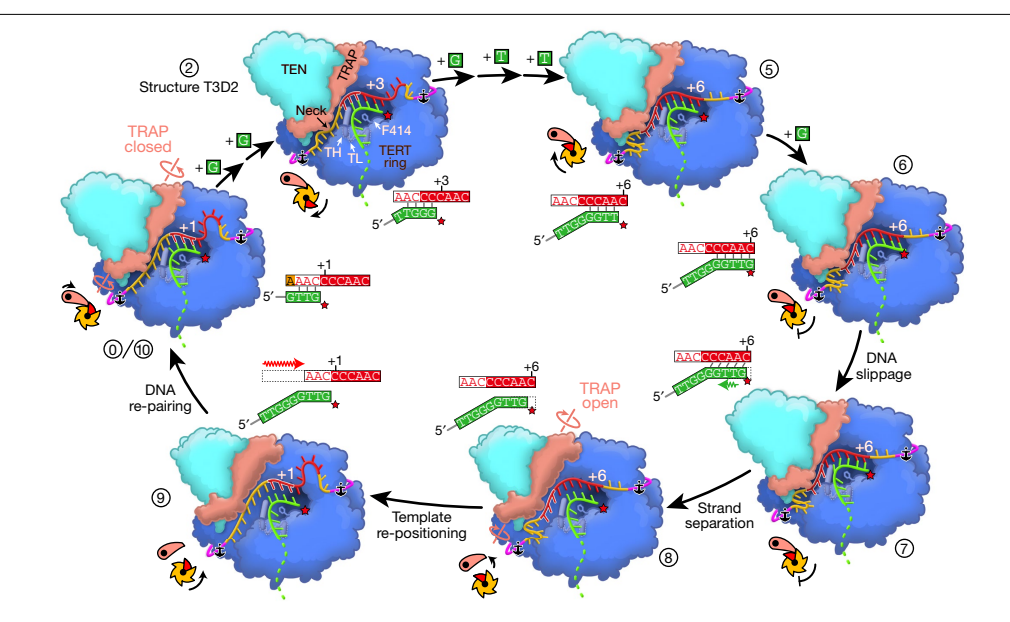


Fig. 4 | Structural details for determining template boundaries. a, Telomerase T3D2 catalytic cavity with TER (grey), DNA (green ribbon) and TERT (coloured surface). b. c. Comparison of TER and template-DNA in telomerase T3D2 (b) and T5D5 (c). Red star marks TERT active site. d-g, Detailed TERT-TER interactions in regions indicated with dashed boxes in a. Hydrogen bonds (dashed yellow lines) and stacking interactions (black lines) are indicated. TRAP-TH channel is shown as electrostatic surface in f. h, Schematic of interactions between TERT and TRE₁-TRE. i, Telomerase activity assays with TERT substitutions on the interface with $TBE_{\scriptscriptstyle I}$ and TRE_I. Telomerase activity and RAP were determined relative to wild type. The data are mean \pm s.d. from three independent experiments.



 $\label{eq:Fig.5} \textbf{Fig. 5} \ | \ A \ model for telomere repeat synthesis.} \ At \ step \ 0 \ (or 10), \ six \ TRE_L \ nucleotides are in the TRAP-TH channel, with three stacked above the neck and three fully stretched between the neck and TRE. Five template nucleotides beyond the +1 position, and two TBE_L nucleotides, are looped out. The template moves from +1 to +6 position during the synthesis of one telomere repeat (steps 0-6), with concomitant stretching of TBE_L and looping of TRE_L. At step 6, the TBE_L is fully stretched and all seven TRE_L nucleotides plus one template nucleotide are looped out below the neck of the TRAP-TH channel. Following$

addition of the final dGTP, a series of events leads to template translocation: duplex distortion (step 7), duplex melting and TRAP opening (step 8), template re-positioning (step 9), and DNA re-pairing and TRAP closing (10). TBE and TRE anchor sites, locations of TH, TL, Phe414, and template position at active site are illustrated. The pawl-and-ratchet cartoons illustrate the movement of TRAP (salmon) and TRE $_{\rm L}$ nucleotides (orange) through the TRAP–TH neck. Step 2 corresponds to the 3.3 Å-resolution structure T3D2.

and Arg921) that interact with the backbone of the final three TER nucleotides in the catalytic cavity. In telomerase T3D2, these are template A_{51} and TRE_L A_{52} and A_{53} (Fig. 4f-h). Below the neck, A_{54} makes a sharp turn from the helical stack, and $TRE_L A_{54}$ to A_{58} form a loop, with A_{54} , C_{56} and A_{58} stacked in and U_{55} and U_{57} flipped out. In telomerase T5D5, all three template alignment nucleotides (C_{49} , A_{59} and A_{51}) are in the TRAP-TH channel (Extended Data Fig. 9d-f). Of the seven TRE nucleotides extruded through the neck, only A₅₂ and A₅₃ are visible in the cryo-EM map; A₅₄ to A₅₈ can apparently no longer be accommodated in the channel and loop out. Individual alanine substitutions of basic residues along the TRAP-TH channel (Fig. 4h) all decrease telomerase activity to less than 25%, while Y694A has a less severe effect (Fig. 4i). Additionally, K657A, R658A and R921A (which are located above the neck) decrease RAP to undetectable levels or to less than 50% (Fig. 4i). These results indicate that the interactions between the positively charged surface of the channel and TRE₁ are essential for regulating telomeric repeat synthesis, and specifically that interactions above the neck are involved in RAP. Together with the constriction at the neck, these interactions may create an energy barrier that prevents backwards movement of TRE₁ nucleotides that have passed through the neck.

Mechanism of telomere repeat synthesis

On the basis of the four sstDNA-bound telomerase structures (especially the highest resolution structures T3D2 and T5D5), we propose a model for telomere repeat synthesis (Fig. 5). The sstDNA initially base pairs with the template alignment region and this short helix is stabilized in the catalytic cavity by the TEN–TRAP above it and by interactions with TH, TL and the bridge loop (step 0 in Fig. 5). As the template moves through the active site during nucleotide addition, the template–TBE_L loop decreases in size while TRE_L nucleotides pushed through the TRAP–TH neck begin to loop out (steps 2 to 5 in Fig. 5). Although tension might accumulate as the TRE_L loop grows⁴⁴, the TRAP–TH neck

acts similarly to a ratchet, preventing the nucleotides that have passed through from moving back.

Following addition of the final telomeric repeat nucleotide (step 6 in Fig. 5), the template has to translocate to its starting position. We propose that repeat translocation could share a fundamental mechanism with nucleotide translocation. Nucleotide translocation intermediates, which were previously captured in structures of a viral RNA dependent-RNA polymerase, suggest an asymmetric movement of the duplex, in which the product strand shifts first (distorting and weakening the base pairs) and then the template strand follows⁴⁵. A similar mechanism could apply to telomerase. However, after addition of the final nucleotide, only the DNA strand can move; the template cannot follow because TBE₁ is fully stretched (step 7 in Fig. 5). This nucleotide-translocation intermediate would destabilize the duplex, contributing to strand separation before template translocation. Movement of the CTE of TERT has previously been proposed to pull the DNA off the template 46,47; however, our structures suggest that CTE rotation would be highly restricted. Instead, TEN-TRAP (which exhibits conformational dynamics (Extended Data Fig. 2d)) could rotate around its two points of contact with the TERT ring-which may be facilitated by the build-up of TRE, nucleotides in the lower part of the TRAP-TH channel—and thus disrupt the narrow channel and release the tension (step 8 in Fig. 5). Then, the template would slip back along motif 3 (Extended Data Fig. 3j) and reset the +1 position at the active site (step 9 in Fig. 5), where TRE_L on the 3' side of the template is fully stretched (Extended Data Fig. 9g). Because TH and TL interact with the sstDNA throughout synthesis (Extended Data Fig. 8), they could hold the DNA backbone during template translocation, consistent with mutagenesis results for human telomerase⁴⁷. Stacking of Phe414 in the bridge loop on the flipped DNA bases could prevent the DNA strand from moving, and thus keep it in position to pair with the template alignment region once more. After the template-DNA duplex reforms, the TRAP-TH channel closes (step 0 and 10 in Fig. 5). This unified mechanism may also explain why primers that contain

locked nucleic acids, which stabilize the nucleotide pre-translocation state, prevent repeat translocation.

Because only a 4-5-bp duplex forms throughout the steps of telomere repeat synthesis (Extended Data Fig. 8), template-DNA strand separation should not require much energy; instead, the duplex needs to be stabilized in the catalytic cavity. We propose that TEN-TRAP and the bridge loop of the RBD have evolved to retain the short templateduplex throughout nucleotide addition as well as to have an essential role in template translocation. Previous modelling has suggested a similar set of TERT-TER interactions for human telomerase⁴⁸. Comparison of p50 OB and TPP1 OB structures and interactions also provides evidence for a conserved TERT interface for telomerase activation and recruitment to telomeres.

p65, the telomerase biogenesis protein of *Tetrahymena*, binds the enclosing stem of the t/PK, the pseudoknot and the stem-terminus element, all of which are common to almost all TERs. Pof8 (a fission yeast LARP7 protein) is a component of telomerase, and has recently been proposed to bind the pseudoknot⁴⁹. In humans, LARP7 deficiency affects telomere length⁵⁰. Together, this suggests that LARP7 may have a common role in TER assembly with TERT. In summary, our results $provide in sights into telomerase \, assembly, the \, mechanism \, of telomeric \,$ repeat synthesis, telomerase recruitment and telomeric DNA handling.

Online content

Any methods, additional references, Nature Research reporting summaries, source data, extended data, supplementary information, acknowledgements, peer review information; details of author contributions and competing interests; and statements of data and code availability are available at https://doi.org/10.1038/s41586-021-03529-9.

- Blackburn, E. H. & Collins, K. Telomerase: an RNP enzyme synthesizes DNA. Cold Spring Harb, Perspect, Biol. 3, a003558 (2011).
- 2 Armanios, M. & Blackburn, E. H. The telomere syndromes. Nat. Rev. Genet. 13, 693-704
- 3. Shay, J. W. Role of telomeres and telomerase in aging and cancer. Cancer Discov. 6, 584-593 (2016).
- Jiang, J. et al. Structure of Tetrahymena telomerase reveals previously unknown subunits, functions, and interactions. Science 350, aab4070 (2015).
- Jiang, J. et al. Structure of telomerase with telomeric DNA. Cell 173, 1179-1190.e13 5.
- 6. Nguyen, T. H. D. et al. Cryo-EM structure of substrate-bound human telomerase holoenzyme. Nature 557, 190-195 (2018).
- 7. Wang, F. et al. The POT1-TPP1 telomere complex is a telomerase processivity factor. Nature 445, 506-510 (2007).
- 8. Xin, H. et al. TPP1 is a homologue of ciliate TEBP- β and interacts with POT1 to recruit telomerase. Nature 445, 559-562 (2007).
- 9. Greider, C. W. & Blackburn, E. H. Identification of a specific telomere terminal transferase activity in Tetrahymena extracts, Cell 43, 405-413 (1985).
- Chan, H., Wang, Y. & Feigon, J. Progress in human and Tetrahymena telomerase structure determination. Annu. Rev. Biophys. 46, 199-225 (2017).
- 11 Wu, R. A., Upton, H. E., Vogan, J. M. & Collins, K. Telomerase mechanism of telomere synthesis. Annu. Rev. Biochem. 86, 439-460 (2017).
- Podlevsky, J. D., Bley, C. J., Omana, R. V., Qi, X. & Chen, J. J. The telomerase database. Nucleic Acids Res. 36, D339-D343 (2008)
- 13. Prathapam, R., Witkin, K. L., O'Connor, C. M. & Collins, K. A telomerase holoenzyme protein enhances telomerase RNA assembly with telomerase reverse transcriptase. Nat. Struct, Mol. Biol. 12, 252-257 (2005).
- Mitchell, J. R., Cheng, J. & Collins, K. A box H/ACA small nucleolar RNA-like domain at the human telomerase RNA 3' end. Mol. Cell. Biol. 19, 567-576 (1999).
- Gillis, A. J., Schuller, A. P. & Skordalakes, E. Structure of the Tribolium castaneum telomerase catalytic subunit TERT. Nature 455, 633-637 (2008).
- Jiang, J. et al. The architecture of Tetrahymena telomerase holoenzyme. Nature 496, 187-192 (2013).
- Lei, M., Podell, E. R. & Cech, T. R. Structure of human POT1 bound to telomeric single-stranded DNA provides a model for chromosome end-protection. Nat. Struct. Mol. Biol. 11. 1223-1229 (2004).
- Lim, C. J. & Cech, T. R. Shaping human telomeres: from shelterin and CST complexes to telomeric chromatin organization. Nat. Rev. Mol. Cell Biol. 22, 283-298

- Lue, N. F., Chan, J., Wright, W. E. & Hurwitz, J. The CDC13-STN1-TEN1 complex stimulates Pol a activity by promoting RNA priming and primase-to-polymerase switch. Nat. Commun 5 5762 (2014)
- Maraia, R. J., Mattijssen, S., Cruz-Gallardo, I. & Conte, M. R. The La and related RNA-binding proteins (LARPs): structures, functions, and evolving perspectives. Wiley Interdiscip. Rev. RNA 8, e1430 (2017).
- Singh, M. et al. Structural basis for telomerase RNA recognition and RNP assembly by the holoenzyme La family protein p65. Mol. Cell 47, 16-26 (2012).
- Stone, M. D. et al. Stepwise protein-mediated RNA folding directs assembly of telomerase ribonucleoprotein. Nature 446, 458-461 (2007).
- Kotik-Kogan, O., Valentine, F. R., Sanfelice, D., Conte, M. R. & Curry, S. Structural analysis reveals conformational plasticity in the recognition of RNA 3' ends by the human La protein, Structure 16, 852-862 (2008).
- Nandakumar, J. et al. The TEL patch of telomere protein TPP1 mediates telomerase recruitment and processivity, Nature 492, 285-289 (2012).
- Zhong, F. L. et al. TPP1 OB-fold domain controls telomere maintenance by recruiting telomerase to chromosome ends. Cell 150, 481-494 (2012).
- Tesmer, V. M., Smith, E. M., Danciu, O., Padmanaban, S. & Nandakumar, J. Combining conservation and species-specific differences to determine how human telomerase binds telomeres. Proc. Natl Acad. Sci. USA 116, 26505-26515 (2019).
- Grill, S., Tesmer, V. M. & Nandakumar, J. The N terminus of the OB domain of telomere protein TPP1 is critical for telomerase action. Cell Rep. 22, 1132-1140 (2018)
- Zhang, Y. et al. Phosphorylation of TPP1 regulates cell cycle-dependent telomerase recruitment. Proc. Natl Acad. Sci. USA 110, 5457-5462 (2013).
- Upton, H. E., Chan, H., Feigon, J. & Collins, K. Shared subunits of Tetrahymena telomerase holoenzyme and replication protein a have different functions in different cellula complexes. J. Biol. Chem. 292, 217-228 (2017).
- Zeng, Z. et al. Structural basis for Tetrahymena telomerase processivity factor Teb1 binding to single-stranded telomeric-repeat DNA. Proc. Natl Acad. Sci. USA 108, 20357-20361 (2011).
- Shastry, S., Steinberg-Neifach, O., Lue, N. & Stone, M. D. Direct observation of nucleic acid binding dynamics by the telomerase essential N-terminal domain. Nucleic Acids Res. 46, 3088-3102 (2018).
- Jansson, L. J. et al. Telomere DNA G-quadruplex folding within actively extending human telomerase, Proc. Natl Acad. Sci. USA 116, 9350-9359 (2019).
- Patrick F M Slivka LD Payne B Comstock M L & Schmidt LC Observation of processive telomerase catalysis using high-resolution optical tweezers. Nat. Chem. Biol. 16, 801-809 (2020).
- 34. Wang, Y., Sušac, L. & Feigon, J. Structural biology of telomerase. Cold Spring Harb. Perspect. Biol. 11, a032383 (2019).
- Xie, M., Podlevsky, J. D., Qi, X., Bley, C. J. & Chen, J. J. A novel motif in telomerase reverse 35 transcriptase regulates telomere repeat addition rate and processivity. Nucleic Acids Res. 38. 1982-1996 (2010).
- Nakamura, T. M. et al. Telomerase catalytic subunit homologs from fission yeast and human, Science 277, 955-959 (1997).
- Jansson, L. I. et al. Structural basis of template-boundary definition in Tetrahymena telomerase. Nat. Struct. Mol. Biol. 22, 883-888 (2015).
- Akiyama, B. M., Gomez, A. & Stone, M. D. A conserved motif in Tetrahymena thermophila telomerase reverse transcriptase is proximal to the RNA template and is essential for boundary definition. J. Biol. Chem. 288, 22141-22149 (2013).
- Harkisheimer, M., Mason, M., Shuvaeva, E. & Skordalakes, E. A motif in the vertebrate telomerase N-terminal linker of TERT contributes to RNA binding and telomerase activity and processivity. Structure 21, 1870-1878 (2013).
- Vester, B. & Wengel, J. LNA (locked nucleic acid): high-affinity targeting of complementary RNA and DNA. Biochemistry 43, 13233-13241 (2004).
- Schaich, M. A. et al. Mechanisms of nucleotide selection by telomerase. eLife 9, e55438 (2020).
- Lai, C. K., Miller, M. C. & Collins, K. Template boundary definition in Tetrahymena telomerase. Genes Dev. 16, 415-420 (2002).
- 43. Miller, M. C. & Collins, K. Telomerase recognizes its template by using an adjacent RNA motif. Proc. Natl Acad. Sci. USA 99, 6585-6590 (2002).
- Berman, A. J., Akiyama, B. M., Stone, M. D. & Cech, T. R. The RNA accordion model for template positioning by telomerase RNA during telomeric DNA synthesis. Nat. Struct. Mol. Biol. 18, 1371-1375 (2011).
- Wang, M. et al. Stringent control of the RNA-dependent RNA polymerase translocation revealed by multiple intermediate structures. Nat. Commun. 11, 2605 (2020).
- 46. Yang, W. & Lee, Y. S. A DNA-hairpin model for repeat-addition processivity in telomere synthesis, Nat. Struct, Mol. Biol. 22, 844-847 (2015).
- Wu, R. A., Tam, J. & Collins, K. DNA-binding determinants and cellular thresholds for human telomerase repeat addition processivity. EMBO J. 36, 1908-1927 (2017).
- Wang, Y., Gallagher-Jones, M., Sušac, L., Song, H. & Feigon, J. A structurally conserved human and Tetrahymena telomerase catalytic core. Proc. Natl Acad. Sci. USA 117, 31078-31087 (2020).
- Hu, X. et al. Quality-control mechanism for telomerase RNA folding in the cell. Cell Rep. 33, 108568 (2020)
- Holohan, B. et al. Impaired telomere maintenance in Alazami syndrome patients with LARP7 deficiency. BMC Genomics 17 (Suppl 9), 749 (2016).

Publisher's note Springer Nature remains neutral with regard to jurisdictional claims in published maps and institutional affiliations.

© The Author(s), under exclusive licence to Springer Nature Limited 2021

Methods

No statistical methods were used to predetermine sample size. The experiments were not randomized, and investigators were not blinded to allocation during experiments and outcome assessment.

Telomerase sample preparation

Tetrahymena thermophila CU522 TERT-FZZ strain with a replacement of the endogenous TERT gene with a C-terminally TAP-tagged (3×FLAG-TEV-ZZ) TERT⁵¹ (provided by K. Collins) was used for telomerase purification. Tetrahymena telomerase was purified following a previously described protocol¹⁶, with minor modifications. Sixteen litres of Tetrahymena TERT-FZZ cells was grown in PPYS medium and collected by centrifugation. The cell pellet was washed with 20 mM HEPES·NaOH pH 8.0, and then lysed in lysis buffer (20 mM HEPES·NaOH pH 8.0, 50 mM NaCl, 1 mM EDTA, 1 mM TCEP, 10% glycerol, 0.2% IGEPAL CA-630, 0.1% Triton X-100) at 4 °C for 30 min. The cell lysate was clarified by $ultracentrifugation \, at \, 230,\!000 g \, for \, 1 \, h. \, After \, ultracentrifugation, the \,$ supernatant of the lysate was incubated with rabbit-IgG agarose slurry (Sigma) overnight at 4 °C. Then, the resin was washed with wash buffer (20 mM HEPES·NaOH pH 8.0, 50 mM NaCl, 1 mM MgCl₂, 1 mM TCEP, 10% glycerol, 0.1% IGEPAL CA-630) and eluted with TEV protease. During the TEV elution step, sstDNA was added to a final concentration of 5 μM to saturate telomerase, and excess sstDNA was washed away in the following steps of purification. The elution fraction from IgG resin was incubated with 30 µl of pre-washed anti-Flag M2 affinity gel (Sigma) for 1h at 4 °C. After that, the anti-Flag resin was washed extensively with wash buffer and eluted using a small volume (30-50 µl) of elution buffer (20 mM HEPES·NaOH pH 8.0, 50 mM NaCl, 1 mM MgCl₂, 1 mM TCEP, 0.1% IGEPAL CA-630) supplemented with 1 mg ml⁻¹3×Flag peptide. Telomerase samples bound with different sstDNA were prepared separately with DNA primers (GTTGGG)₅ (telomerase T3D2), (GTTGGG)₂GTTGG^LG^LT (telomerase T4D4), and (GTTGGG)₂GTTGGG^LG^LT^LT (telomerase T5D5), in which T^L/G^L represents locked nucleic acid (LNA) oligonucleotide (Exigon).

Cryo-EM specimen preparation and data collection

For cryo-EM sample, 3 μ l of the purified telomerase was applied to glow-discharged lacey carbon grids with a supporting ultrathin carbon film (Ted Pella). The grids were then blotted with filter paper and flash-frozen in liquid ethane using an FEI Vitrobot Mark IV. Cryo-EM grids were screened in an FEI Tecnai TF20 transmission electron microscope while optimizing freezing conditions.

Vitrified cryo-EM grids were loaded into an FEI Titan Krios electron microscope at 300 kV for automated image acquisition with SerialEM 52 . Movies of dose-fractionated frames were acquired with a Gatan K2 Summit direct electron detector operated in super-resolution mode, yielding a pixel size of 0.68 Å on the sample level). A Gatan imaging filter was installed between the electron microscope and the K2 camera with the slit width setting to 20 eV. The electron microscope was carefully aligned before each imaging session and the parallel beam was optimized using coma-free alignment in SerialEM 52 . The dose rate on the detector was set to about 6 electrons per $\mathring{\rm A}^2$ per s and the total exposure time of each movie was 8 s, which fractionated into 40 frames of images with 0.2-s exposure time for each frame. In total, 13,097 movies for telomerase T3D2, 5,020 movies for telomerase T4D4, and 12,922 movies for telomerase T5D5 were collected in separate imaging sessions.

Cryo-EM data processing of telomerase T3D2

Dose-fractionated frames except for the first of each movie were 2×10^{13} binned (pixel size of 1.36 Å) and aligned for correction of beam-induced drift using MotionCor2⁵³. Two averaged images, one with dose weighting and the other without, were generated after drift correction. The averaged micrographs without dose weighting were used for the determination of contrast transfer function (CTF) parameters and

particle picking, and the averaged micrographs with dose weighting were used for particle extraction and further data processing. The defocus and astigmatism values of each micrograph were determined by CTFFIND4 54 . All micrographs after motion correction and their power spectra were visually inspected, and the micrographs with too much thick carbon area, ice contamination or defocus value outside the range from -0.8 to $-4.0~\mu m$ were discarded. Finally, a total of 10,849 micrographs were kept.

Particles in those averaged images were automatically picked with Gautomatch (www.mrc-lmb.cam.ac.uk/kzhang/) using 17 projections from previously reported cryo-EM map of *Tetrahymena* telomerase (Electron Microscopy Data Bank (EMDB) code EMD-7821) 5 . To avoid losing good particles on the low-contrast micrographs collected with carbon-coated cryo-EM grids, we used a low threshold for particle picking (over 350 particles on each micrograph) and then used a previously developed data processing protocol 5 to select good particles (as detailed in the following paragraph). Finally, a total of 3,816,856 particles were picked, extracted in dimensions of 256 × 256 square pixels and 2×-binned to 128 × 128 square pixels (pixel size of 2.72 Å) to speed up the following data processing with RELION 3.0 (Ref. 55).

The cryo-EM data processing procedure is outlined in Extended Data Fig. 2a. Two datasets (one for each data collection session) were initially processed separately in two batches. For each dataset, extracted particles were classified into six subsets using 3D classification. The previously reported DNA-bound telomerase density map (EMD-7821) was low-pass-filtered to 60 Å before using as the initial model. The particles in each 3D class were then classified into 100 classes using reference-free 2D classification. Particles in 2D classes with fuzzy or uninterpretable features were discarded, and most of them were pure noise from background carbon film instead of real telomerase particles. By doing the above 3D and 2D classification steps, we could keep more particles that were in the rare views. After the initial particle screening step, a total of 1,015,378 particles (26.6% of all particles) were combined, recentred and re-extracted from dose-weighted micrographs in dimensions of 256×256 square pixels (pixel size of 1.36 Å). From those re-extracted particles, 945,254 particles (24.8% of all particles) were further selected using an additional round of 2D classification. Refinement of those particles with a spherical mask generated a 3D reconstruction with clear secondary structure features for the majority of telomerase (including TERT-TER-p65 core, p50 OB and TEB subcomplex) and weak density for the flexible p75-p45-p19 subcomplex, which could only be partially observed at a lower threshold of the density map (CL = 3σ). To improve the overall resolution, a soft mask (mask 1) was used to exclude the flexible p75-p45-p19 subcomplex during the following data processing. Then, we performed another round of 3D classification with local angular search (RELION options:--sigma_ang 12), using the orientation parameters determined by the above 3D refinement as inputs. The particles were classified into six classes, and those in the two good classes with clear features for the catalytic core were selected. Refinement of the combined 466,385 particles (12.2% of all particles) from the 2 good classes generated an overall 3.3 Å-resolution reconstruction with variable local resolutions within the map. An additional round of 3D classification with a higher regularization parameter T (RELION options:--tau2_fudge 10 --sigma_ang 12) was performed to separate the movements of the TEN-TRAP region. Refinement of particles in the three major classes generated three reconstructions (P1, P2 and P3) with their TEN-TRAP at slightly different positions relative to the TERT ring (Extended Data Fig. 2d). We then refined the 193,117 particles in the P2 class again, followed by several rounds of CTF refinement to correct the CTF parameters, anisotropic magnification and higher-order aberrations. Beam-induced particle motion was corrected in RELION3.0 using Bayesian polishing module. The resulted 'shiny' particles were refined with mask 1, resulting in a final 3.3 Å-resolution reconstruction with improved overall densities. To improve local resolution for model building, focused 3D classifications

without alignment (RELION options:--skip_align --tau2_fudge 10) were performed using soft masks separately around the pseudoknot-La motif and Teb3, followed by 3D refinements with mask 1. The resulting two reconstructions and the 3.3 Å-resolution reconstruction were used for model building, as detailed below.

Resolutions of the cryo-EM maps were estimated on the basis of the 'gold-standard' Fourier shell correlation (FSC) = 0.143 criterion. The cryo-EM maps were corrected for the modulation transfer function of the detector, sharpened with a negative B-factor and low-pass filtered to the stated resolution using the relion_postprocess program in RELION. Local-resolution evaluations were determined by ResMap. With two independently refined half-maps. Data collection and processing statistics are given in Extended Data Table 1.

Cryo-EM data processing of telomerase T4D4 and T5D5

For telomerase T4D4, 1,749,767 particles were picked from 4,885 micrographs. We then selected 111,603 particles by procedures similar to those described above for telomerase T3D2. To separate DNA-bound and DNA-free particles, an additional round of focused 3D classification without alignment (RELION options:--skip_align --tau2_fudge 10) was performed using a spherical mask surrounding the template-DNA duplex region. Finally, a 4.4 Å-resolution reconstruction with clear duplex density was generated with selected 28,297 DNA-bound particles (Extended Data Fig. 7c). For telomerase T5D5, 3,951,672 particles were picked from 11,612 micrographs. We selected 120,360 DNA-bound particles, which yielded a 3.8 Å-resolution reconstruction (Extended Data Fig. 7d). By using a smaller spherical mask surrounding the template-DNA duplex region during focused 3D classification (RELION options:--skip align --tau2 fudge 20), we could further separate these DNA-bound particles into two subsets: 51,617 particles with a shorter duplex and 68,743 particles with a longer duplex (Extended Data Fig. 7d). Overall and local resolutions of the T4D4 and T5D5 reconstructions were evaluated as described for telomerase T3D2.

Model building and refinement

The atomic model of telomerase T3D2 was built and refined manually in COOT⁵⁸. Initially, the previously reported model (PDB 6D6V) generated based on a 4.8 Å-resolution cryo-EM map⁵ was fitted into the current 3.3 Å-resolution cryo-EM map with UCSF Chimera⁵⁹ as the starting point for the model building. With the aid of high-resolution features, we manually adjusted side chain conformation of TERT (when necessary) moved the main chain to ensure a close fit between the density and the model. Sequence assignment of TRAP and CTE were mainly guided by visible densities of amino acid residues with bulky side chains, such as Phe, Tyr and Trp. However, the flexible linker between TEN and RBD (amino acids 180-215) was invisible and could not be modelled, as well as two linkers within RBD (amino acids 252-280) and TRAP (amino acids 664–686). Modelling of the TEB subcomplex, including Teb1C (amino acids 511–697), Teb2N (amino acids 29–175) and Teb3 (amino acids 5-121), was achieved in similar way. The main chain of p50 OB (amino acids 1–184) was manually retraced and de novo built with the help of secondary structure prediction generated by PSIPRED⁶⁰. The C-terminal region of p50 (amino acids 185-249) is masked out at least in part along with p75-p45-p19 subcomplex during cryo-EM data processing. Homology model of La motif of p65 (amino acids 114-238) was generated using PHYRE261 and manually adjusted according to the cryo-EM map, including the removal of an invisible internal linker (amino acids 170-201).

TER was initially modelled piece by piece, and then connected manually in COOT. For the regions contacting TERT, including the t/PK and the distal part of stem-loop 4, well-defined nucleotide densities facilitated the de novo model building process. For the rest of TER, including stem-loop 1 and the proximal part of stem-loop 4, previous model (PDB 6D6V) was adjusted for their base conformation and (when necessary) for their backbones to fit into the density map. The apical

loop of stem-loop 2 was modelled with the help of its NMR structure (PDB 2M22)⁶².

The cryo-EM density of telomeric DNA was traced from its 3′ end all the way to Teb1C (Extended Data Fig. 6e, f). Eight nucleotides were modelled unambiguously inside the catalytic cavity, including G_{30} to T_{27} (which pair with the template) and T_{26} to G_{23} (which stack with TERT Phe414). Nucleotides densities binding to the C-shaped cleft of Teb1C could be assigned to three guanosines instead of thymidine according to their size and shape (Extended Data Fig. 6g, h). Eventually, we modelled them as G_{19} to G_{17} as the weak density connecting them to G_{23} fitted better with a flexible linker of three instead of four nucleotides (Extended Data Fig. 6e). Nucleotides from G_{16} to G_{1} were invisible in the cryo-EM map.

The model obtained above was used as the starting point for the modelling of other lower-resolution reconstructions. The model was first rigid-body fitted into these maps using Chimera and then manually checked in COOT. The template–DNA duplex and adjacent TBE $_{\! L}$ and TRE $_{\! L}$ regions were manually adjusted to fit the densities. On the basis of the knowledge gained from the 3.3 Å-resolution T3D2 structure, the template–DNA duplex in the previously published model of telomerase with (GTTGGG) $_2$ GT $^{\rm L}$ G $^{\rm L}$ GG (telomerase T3D3, PDB 6D6V) was re-evaluated, and new modelling showed a 5-bp template–DNA duplex (Extended Data Fig. 8).

All models were refined using Phenix 63 in real space with secondary structure, Ramachandran and rotamer restraints. The structures were validated using the Molprobity scores and statistics of the Ramachandran plots. Refinement statistics of the models were summarized in Extended Data Table 1. Model versus map FSC validation was shown in Extended Data Fig. 2f. Visualization of the atomic models, including figures and movies, were prepared using UCSF Chimera 59 and Chimera 64 .

In vitro transcription and purification of TER

TER was in vitro-transcribed with a linearized DNA template containing a hammerhead ribozyme sequence at the 3' end to allow self-cleavage of TER at a precise position after the transcription 65 . In brief, homemade T7 RNA polymerase was added to a reaction containing 40 mM MgCl $_2$, 4–6 mM of each NTP and 1 μ M DNA template in 40 mM Tris·HCl pH 8.0, 1 mM spermidine, 2.5 mM DTT and 0.01% Triton X-100. The reaction was incubated overnight at 37 °C for transcription of the DNA template and cleavage of the hammerhead ribozyme construct. TER was subsequently purified by electrophoresis on a 10% denaturing polyacrylamide gel followed by electroelution of the excised RNA band 66 .

In vitro reconstitution of telomerase and direct activity assays

The expression and assembly of telomerase was performed in vitro in rabbit reticulocyte lysates (RRL) as previously described^{4,67}, with minor changes. TERT and p65 were co-expressed using TNT quick-coupled transcription and translation systems (Promega) in the presence of TER. The expression of TERT was monitored by 35S-methionine incorporation. p50N30 (amino acids 1-251) was expressed in another RRL synthesis reaction. Teb1C (amino acids 505–701) was expressed in E. coli and purified by size-exclusion chromatography before use. The expressed TERT-TER-p65 core, p50N30 and Teb1C were incubated together in RRL at 30 °C for 30 min before activity assays. The final concentrations of TER and Teb1C in the RRL mixtures were 370 nM and 450 nM, respectively. The activity assay was carried out in a 20 µl solution containing 200 μ M dTTP, 3 μ M dGTP, 5–10 μ Ci dGTP[α^{32} P] (Perkin-Elmer), 2 mM Mg²⁺, 10 μM (GTTGGG)₅ primer and 10 μl RRL mixture. Reactions were performed at 30 °C for 15 min and stopped with quench buffer (10 mM Tris·HCl pH 8.0 and 10 mM EDTA). The products were phenol-chloroform-extracted and ethanol-precipitated together with a 15 nt ³²P-end-labelled DNA oligonucleotide as a recovery control and resolved on a 10% denaturing polyacrylamide gel. The gel was dried and exposed to a phosphor imaging screen and scanned on a PharosFX system (Bio-Rad).

Band intensities were quantified using QuantityOne software (Bio-Rad). Relative activities of TERT mutations were determined by normalizing the integrated density of each lane relative to the recovery control then comparing to that of wild-type TERT (as 100%). Relative RAP of TERT mutations were determined by the 'fraction left behind' (FLB) method^{32,68}. For each lane, the counts for each RAP band, which represented the extension of one telomere repeat, were divided by the number of radioactive guanosines incorporated and normalized against the recovery control. Then, the FLB of each RAP band was calculated by taking the sum of counts for each RAP band and all RAP bands below it divided by the total counts of RAP bands in this lane. Then, the ln(1-FLB) of each RAP band was plotted against repeat number added and the scattered points were fitted with a linear regression to get the slope value. Finally, the relative RAP for each mutation was determined by -ln(2)/slope and compared to that of wild type (as 100%). Activity assays for each TERT mutation were repeated 3 or 4 times.

Reporting summary

Further information on research design is available in the Nature Research Reporting Summary linked to this paper.

Data availability

Cryo-EM density maps have been deposited in the EMDB under accession numbers EMD-23437 (telomerase T3D2), EMD-23438 (telomerase T4D4) and EMD-23439 (telomerase T5D5). The atomic models have been deposited in the PDB under accession codes 7LMA (telomerase T3D2) and 7LMB (telomerase T5D5). The atomic model and cryo-EM density map of telomerase T3D3 were retrieved from the PDB (accession code 6D6V) and EMDB (accession code EMD-7821). Other structures used in this study were retrieved from the PDB with accession codes 2146 (TPP1 OB), 3KYL (*Tribolium* TERT-like protein) and 2M22 (TER stem-loop 2). Uncropped version of all the gels are included as Supplementary Fig. 1. Any other relevant data are available from the corresponding authors upon reasonable request.

- Min, B. & Collins, K. An RPA-related sequence-specific DNA-binding subunit of telomerase holoenzyme is required for elongation processivity and telomere maintenance. *Mol. Cell* 36, 609–619 (2009).
- Mastronarde, D. N. Automated electron microscope tomography using robust prediction of specimen movements. J. Struct. Biol. 152, 36–51 (2005).
- Zheng, S. Q. et al. MotionCor2: anisotropic correction of beam-induced motion for improved cryo-electron microscopy. Nat. Methods 14, 331–332 (2017).
- Rohou, A. & Grigorieff, N. CTFFIND4: fast and accurate defocus estimation from electron micrographs. J. Struct. Biol. 192, 216–221 (2015).
- Zivanov, J. et al. New tools for automated high-resolution cryo-EM structure determination in RELION-3. eLife 7, e42166 (2018).
- Rosenthal, P. B. & Henderson, R. Optimal determination of particle orientation, absolute hand, and contrast loss in single-particle electron cryomicroscopy. J. Mol. Biol. 333, 721–745 (2003).

- Kucukelbir, A., Sigworth, F. J. & Tagare, H. D. Quantifying the local resolution of cryo-EM density maps. Nat. Methods 11. 63–65 (2014).
- Emsley, P., Lohkamp, B., Scott, W. G. & Cowtan, K. Features and development of Coot. Acta Crystallogr. D 66, 486–501 (2010).
- Pettersen, E. F. et al. UCSF Chimera—a visualization system for exploratory research and analysis. J. Comput. Chem. 25, 1605–1612 (2004).
- Buchan, D. W., Minneci, F., Nugent, T. C., Bryson, K. & Jones, D. T. Scalable web services for the PSIPRED protein analysis workbench. *Nucleic Acids Res.* 41, W349–W357 (2013).
- Kelley, L. A., Mezulis, S., Yates, C. M., Wass, M. N. & Sternberg, M. J. The Phyre2 web portal for protein modeling, prediction and analysis. Nat. Protoc. 10, 845–858 (2015).
- Richards, R. J., Theimer, C. A., Finger, L. D. & Feigon, J. Structure of the Tetrahymena thermophila telomerase RNA helix II template boundary element. Nucleic Acids Res. 34, 816–825 (2006).
- Adams, P. D. et al. PHENIX: a comprehensive Python-based system for macromolecular structure solution. Acta Crystallogr. D 66, 213–221 (2010).
- Goddard, T. D. et al. UCSF ChimeraX: meeting modern challenges in visualization and analysis. Protein Sci. 27, 14–25 (2018).
- Cash, D. D. & Feigon, J. Structure and folding of the Tetrahymena telomerase RNA pseudoknot. Nucleic Acids Res. 45, 482–495 (2017).
- Petrov, A., Wu, T., Puglisi, E. V. & Puglisi, J. D. RNA purification by preparative polyacrylamide gel electrophoresis. Methods Enzymol. 530, 315–330 (2013).
- Hong, K. et al. Tetrahymena telomerase holoenzyme assembly, activation, and inhibition by domains of the p50 central hub. Mol. Cell. Biol. 33, 3962–3971 (2013).
- Latrick, C. M. & Cech, T. R. POT1-TPP1 enhances telomerase processivity by slowing primer dissociation and aiding translocation. EMBO J. 29, 924–933 (2010).
- Chu, T. W., D'Souza, Y. & Autexier, C. The insertion in fingers domain in human telomerase can mediate enzyme processivity and telomerase recruitment to telomeres in a TPP1-dependent manner. Mol. Cell. Biol. 36, 210–222 (2015).
- Papadopoulos, J. S. & Agarwala, R. COBALT: constraint-based alignment tool for multiple protein sequences. *Bioinformatics* 23, 1073–1079 (2007).
- Jacobs, S. A., Podell, E. R. & Cech, T. R. Crystal structure of the essential N-terminal domain of telomerase reverse transcriptase. Nat. Struct. Mol. Biol. 13, 218–225 (2006).

Acknowledgements This work was supported by NIH R35GM131901 and NSF MCB2016540 grants to J.F. and NIH grant GM071940 to Z.H.Z. We acknowledge use of instruments at the Electron Imaging Center for Nanomachines supported by UCLA and by instrumentation grants from NIH (1S10RR23057, 1S100D018111 and U24GM116792) and NSF (DBI-1338135 and DMR-1548924). Some preliminary data were collected at the Stanford-SLAC Cryo-EM Center (S2C2) supported by the NIH Common Fund Transformative High Resolution Cryo-Electron Microscopy programme (U24 GM129541) and National Center for CryoEM Access and Training (NCCAT) and the Simons Electron Microscopy Center located at the New York Structural Biology Center, supported by the NIH Common Fund Transformative High Resolution Cryo-Electron Microscopy programme (U24 GM129539), and by grants from the Simons Foundation (SF349247) and NY State Assembly. We thank D. Weisman for help with illustration of Fig. 5.

Author contributions J.F. and Z.H.Z. supervised the project; Y.H. purified telomerase samples, screened cryo-EM grids, and performed cryo-EM data collection and processing; Y.H. and Y.W. built atomic models; Y.H. and B.L. performed telomerase activity assays; C.H., L.S. and R.C. helped with telomerase sample preparation; Y.H. and J.F. wrote the manuscript. All authors contributed to the final version.

Competing interests The authors declare no competing interests.

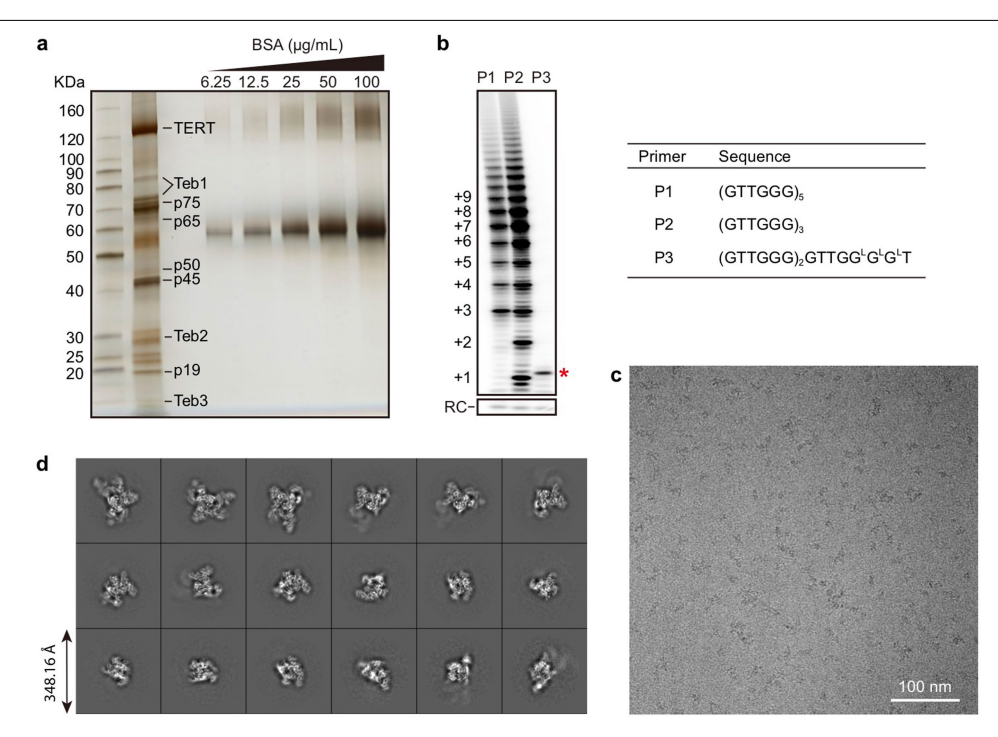
Additional information

 $\textbf{Supplementary information} \ The online version contains supplementary material available at https://doi.org/10.1038/s41586-021-03529-9.$

Correspondence and requests for materials should be addressed to Z.H.Z. or J.F.

Peer review information Nature thanks the anonymous reviewer(s) for their contribution to the peer review of this work. Peer reviewer reports are available.

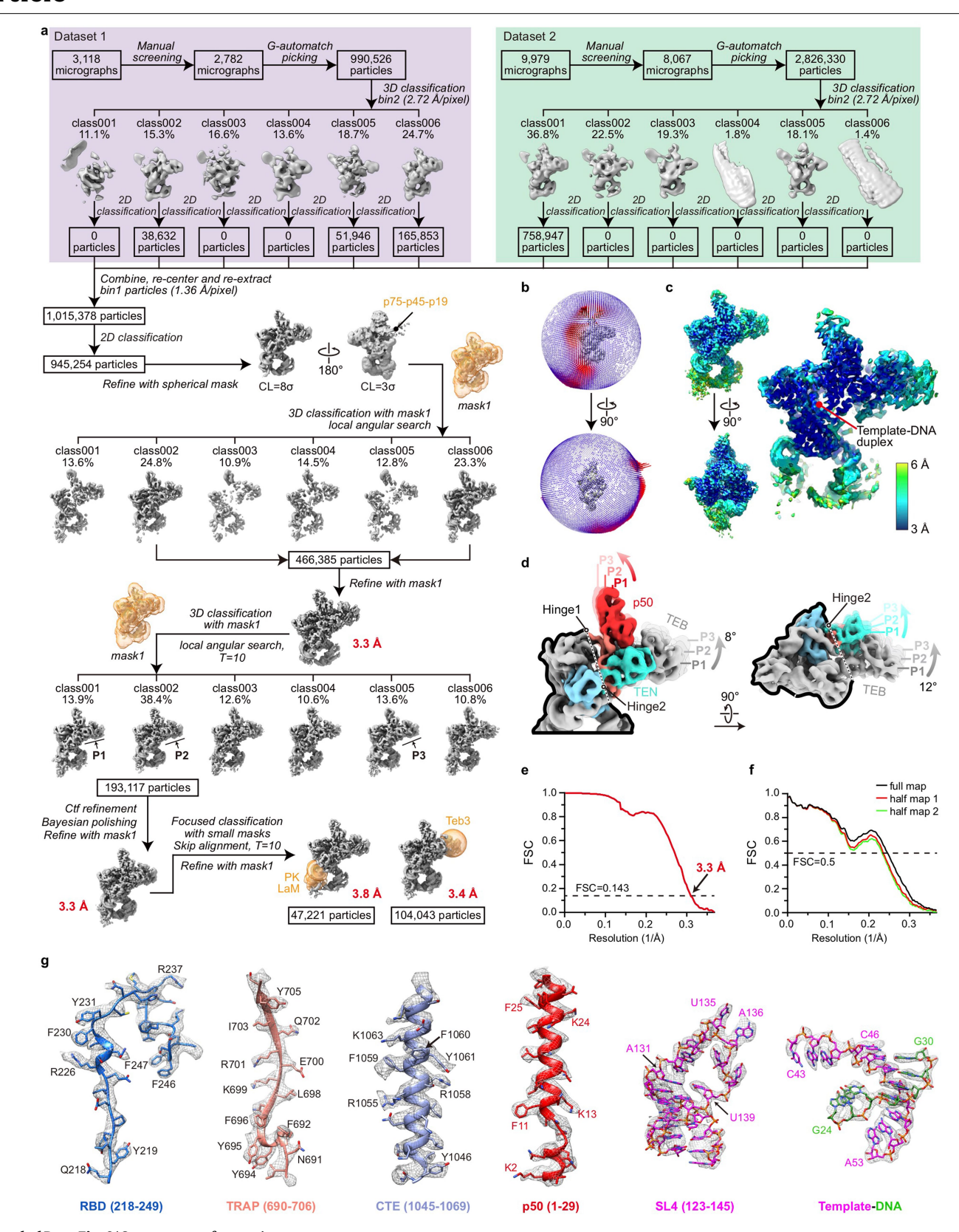
Reprints and permissions information is available at http://www.nature.com/reprints.



Extended Data Fig. 1 | Biochemical and biophysical evaluation of endogenously purified Tetrahymena telomerase with sstDNA.

 $\label{eq:approx} \textbf{a}, Silver-stained SDS-PAGE gel of the tandem-affinity-purified telomerase. Serial diluted BSA samples were loaded together to assist concentration estimation of the telomerase sample. Gel image is representative of independent biological replicates (n = 3). \textbf{b}, Direct telomeric DNA extension assays of the purified telomerase bound with different sstDNA primers. A standard telomera addition pattern is observed when using a (GTTGGG)_5 or (GTTGGG)_3 primer (P1 and P2). However, the translocation of product is$

inhibited when using $(GTTGGG)_2GTTGG^1G^1G^1T$ primer (P3), resulting in a single dark band (red asterisk). G^1 denotes an LNA nucleotide instead of a DNA nucleotide. The LNA-containing product (red asterisk) migrates slightly slower through the gel as compared to nonmodified DNA. Gel image is representative of independent biological replicates (n=3). \mathbf{c} , Motion-corrected cryo-EM micrograph. \mathbf{d} , Representative 2D class averages of telomerase particles. All results from sample purification (\mathbf{a}), activity assays (\mathbf{b}) and cryo-EM experiments (\mathbf{c}) were successfully reproduced at least three times. For gel source data, see Supplementary Fig. 1.



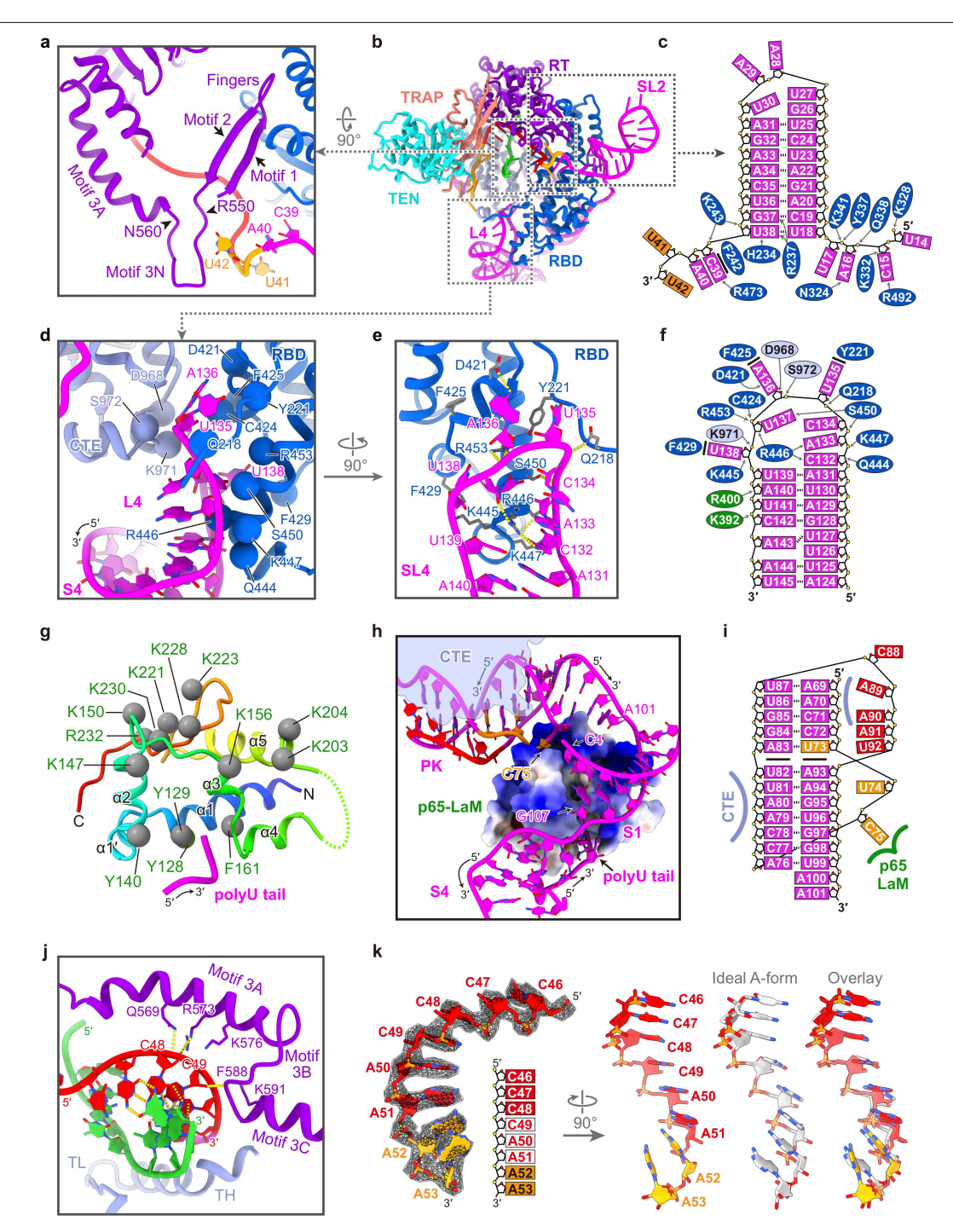
 $\textbf{Extended Data Fig. 2} | See \ next \ page \ for \ caption.$

Extended Data Fig. 2 | Cryo-EM data processing workflow of telomerase with sstDNA (GTTGGG)₅ (telomerase T3D2) and the evaluation of the reconstruction. a, Data processing workflow (detailed in Methods).

Soft masks used in data processing are coloured in orange. b, Euler angle distributions of telomerase particles used for the 3.3 Å-resolution reconstruction. c, Local resolution evaluation of the 3.3 Å resolution cryo-EM map shown in surface views (left) and a slice view of the core region (right).

d, Superposition of reconstructions P1, P2 and P3 that illustrates the rotation of TEN-TRAP. The three maps were low-pass-filtered to 6 Å and aligned on the

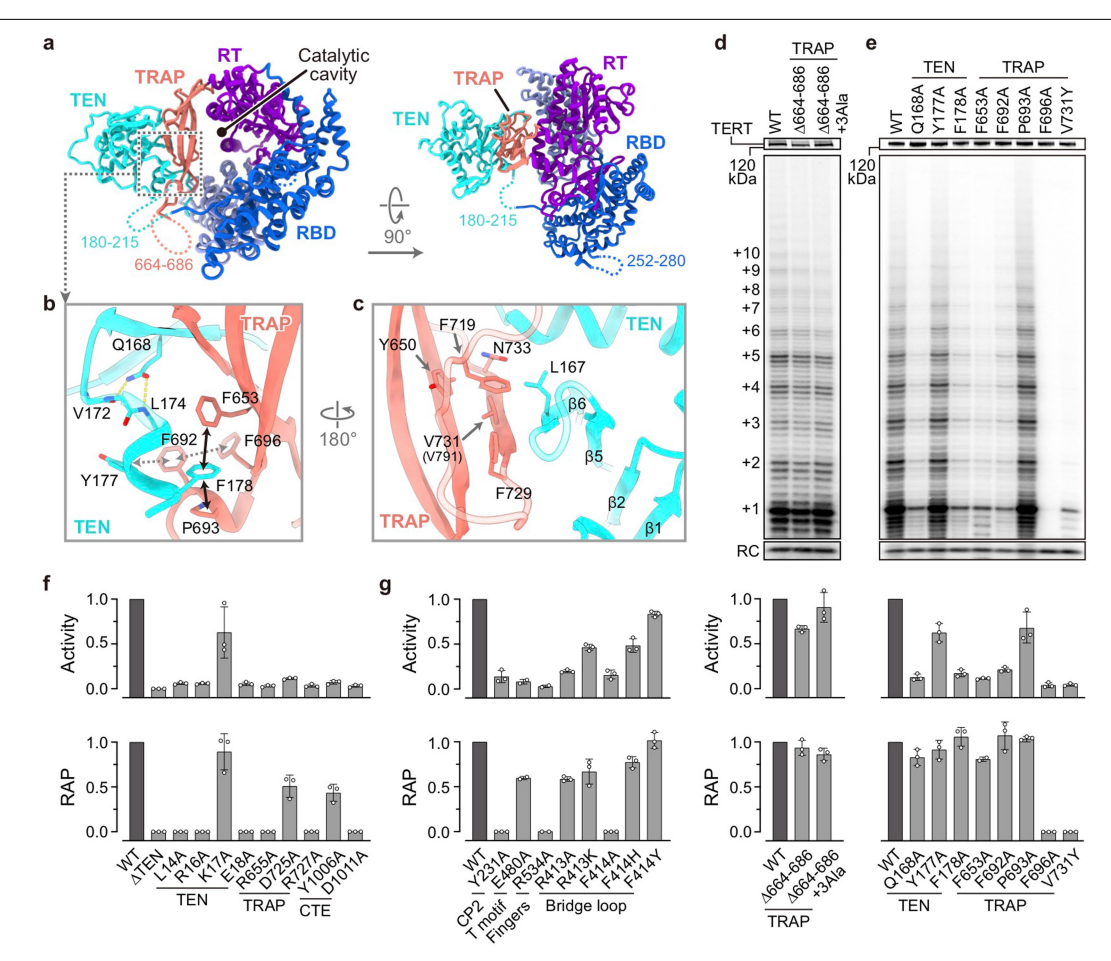
TERT ring. p50 (red) and TEB bind to and move together with TEN-TRAP. \mathbf{e} , Plot of the FSC as a function of the spatial frequency, with resolution of the final reconstruction indicated. \mathbf{f} , FSC coefficients as a function of spatial frequency between model and cryo-EM density maps. Red curve, refined model versus half map 1 used for refinement; green curve, refined model versus half map 2 not used for refinement; black curve, refined model versus the combined final map. The generally similar appearances between the red and green curves suggests no substantial over-fitting. \mathbf{g} , Representative cryo-EM densities (grey and mesh) encasing the related atomic models (colour sticks and ribbons).



$Extended\,Data\,Fig.\,3\,|\,Detailed\,interactions\,between\,TERT\,and\,p65\,with$

TER. a, Close-up view of motif 3N (amino acids 550–560). Motif 3A helix is bent towards motif 2, and motif 3N in between forms a finger-shaped architecture. **b**, Ribbon diagram of the TERT–TER 'interlock' with TERT domains coloured as indicated. **c**, Schematic of stem-loop 2, TBE and TBE $_{\rm L}$ nucleotides and their interactions with RBD of TERT. Arrows indicate sites of polar interactions. Bold line represents the stacking interaction between Phe242 and C $_{39}$. **d**–**f**, Structure of TER loop 4 and its interactions with RBD and CTE of TERT and xRRM of p65 (green). **g**, Rainbow-coloured ribbon diagram of La motif of p65 with secondary structural elements labelled. Positively charged and aromatic residues located on the interface between the La motif of p65 and TER are shown as spheres.

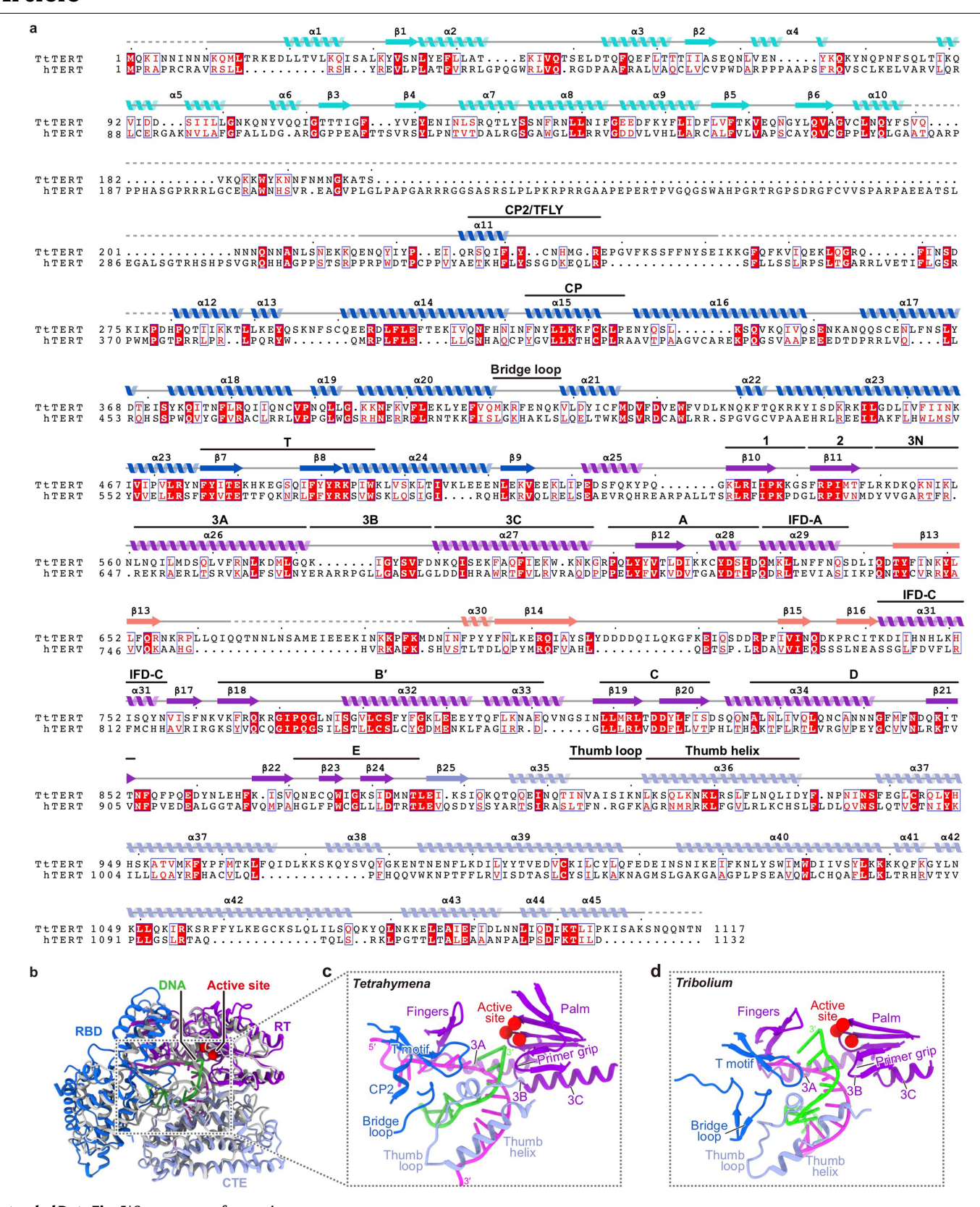
 $\label{eq:hambers} \textbf{h}, \textit{Electrostatic surface representation of the La motif of p65 and its interactions with TER stem 1, pseudoknot and the 3' poly-U. The La motifs of p65 in <math display="inline">\textbf{g}$ and h are in the same orientation. i, Schematic of pseudoknot with regions that interact with TERT and p65 indicated. j, Interactions between motif 3 and the template. End of motif 3B and start of motif 3C are in the minor groove of the duplex. k, The eight TER nucleotides that stack inside the catalytic cavity. Cryo-EM densities are shown as transparent meshes. Ideal A-form stacking of eight nucleotides (white) is shown for comparison. Backbone of the final three TER nucleotides in the stacking deviate from ideal A-form conformation.



Extended Data Fig. 4 | Interactions between TEN-TRAP and telomerase activity assays. a, Ribbon representation of TERT with its domains coloured as indicated. Unmodelled regions of TERT are shown as dashed lines, including the linker between TEN and RBD (amino acids 180–215), flexible linkers within RBD (amino acids 252–280), and TRAP (amino acids 664–686). b, Hydrophobic interactions between the distal region of TRAP and the C-terminal helix of TEN domain, which is further stabilized by Gln168 via two hydrogen bonds. c, The extended β -sheet across TEN and TRAP. V791Y (Val791 in human corresponds

to Val731 in Tetrahymena) mutation in human TERT that disrupts telomere length maintenance and cell immortalization is located at the interface 69 . \mathbf{d} , \mathbf{e} , In vitro-reconstituted telomerase activity assays with TERT mutations on the TEN-TRAP interface. The top panels are SDS-PAGE gels showing the expression level of 35 S-Met incorporated TERT mutants. Quantification of activity and RAP for each mutant are shown in bar graphs below.

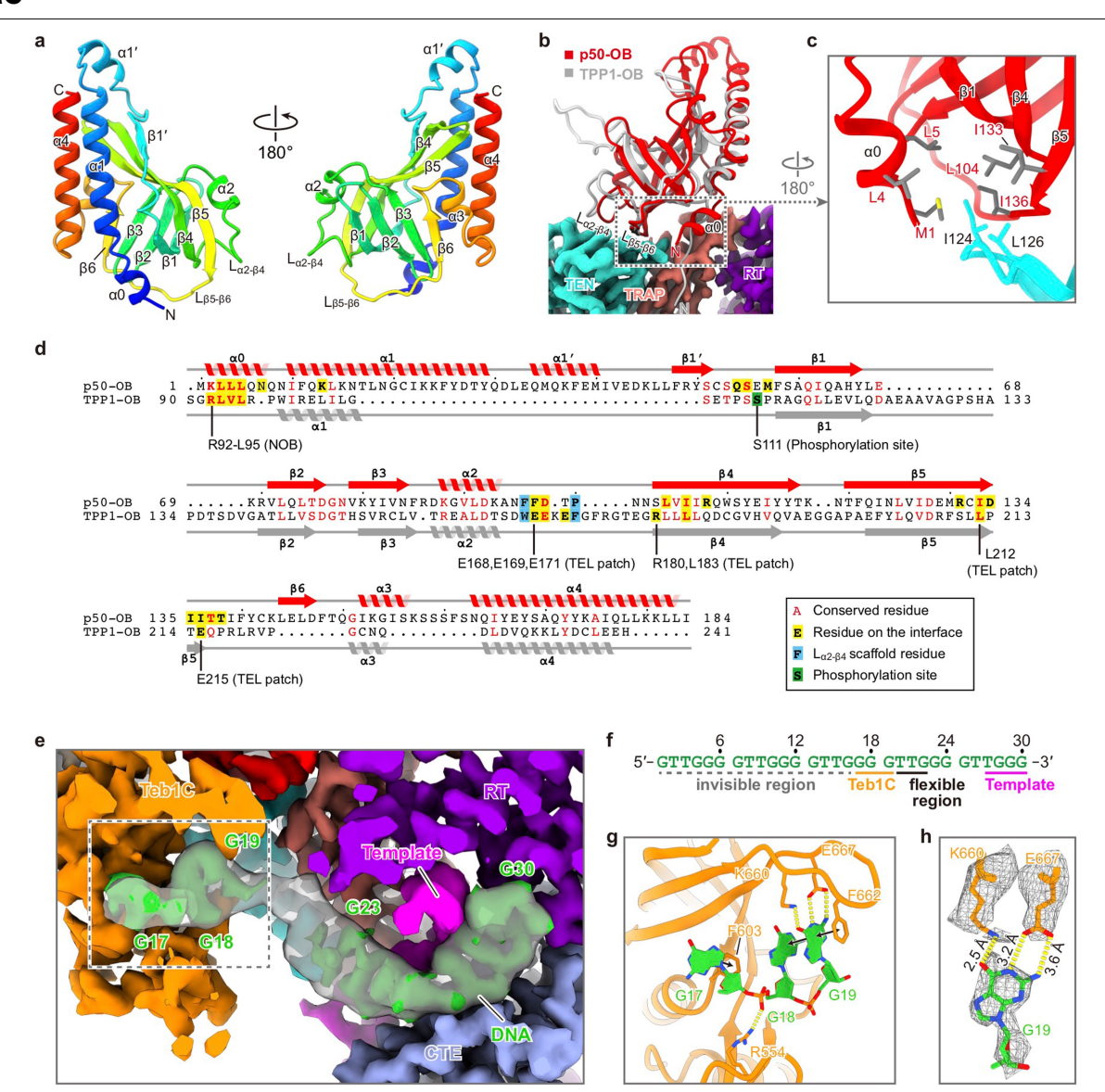
 $\label{eq:fight} \textbf{f}, \textbf{g}, Quantification of activity and RAP for gel shown in Figs. 1j, 3g. Data are mean <math display="inline">\pm$ s.d. from three independent experiments.



Extended Data Fig. 5 | See next page for caption.

Extended Data Fig. 5 | Comparison between TERT from *Tetrahymena* **and human, and the TERT-like protein from** *Tribolium castaneum.* **a.**, Sequence alignment of *Tetrahymena* TERT (TtTERT) human TERT (hTERT). Secondary structures and conserved motifs of *Tetrahymena* TERT are shown on top, with unmodelled regions shown as dashed lines. The alignments of the TEN, RBD, reverse transcriptase and CTE domains and TRAP motif were conducted separately with NIH COBALT⁷⁰ and then merged together. The alignment of CP2 and TFLY region was adjusted manually according to the previously reported alignment ³⁷. **b**, Structural comparison of the TERT-ring of *Tetrahymena* TERT (colour) and *Tribolium* TERT-like protein (grey) (PDB 3KYL). *Tribolium* TERT-like

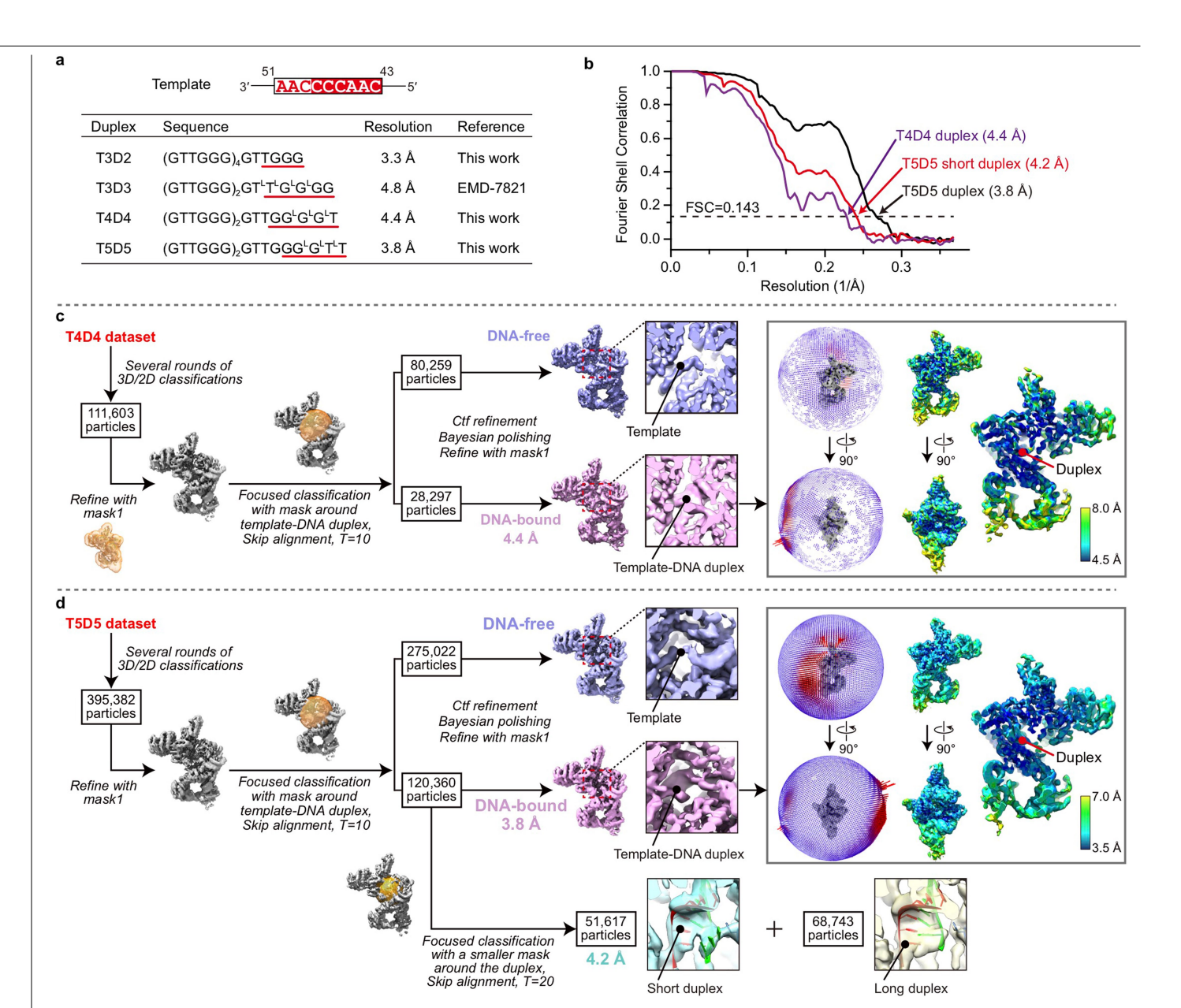
protein lacks TEN, TRAP and TER, and was crystallized with an artificial template–DNA duplex. **c**, **d**, Ribbon diagrams of template–DNA duplexes and surrounding structural elements of *Tetrahymena* TERT (**c**) and *Tribolium* TERT-like protein (**d**). The palm, fingers, primer grip, TH, TL, motif 3 and T are structurally conserved between *Tetrahymena* TERT and *Tribolium* TERT-like protein. The 'bridge loop' of *Tribolium* TERT-like protein is in a similar position to that in *Tetrahymena* TERT; however, the tip residues (Ser82 and Phe83) have no contact with the template–DNA duplex. CP2, which participates in template 5' boundary definition and template nucleotide guidance in *Tetrahymena* TERT, appears to be absent in *Tribolium* TERT-like protein.



Extended Data Fig. 6 | Details of p50 OB-TERT and Teb1C-sstDNA

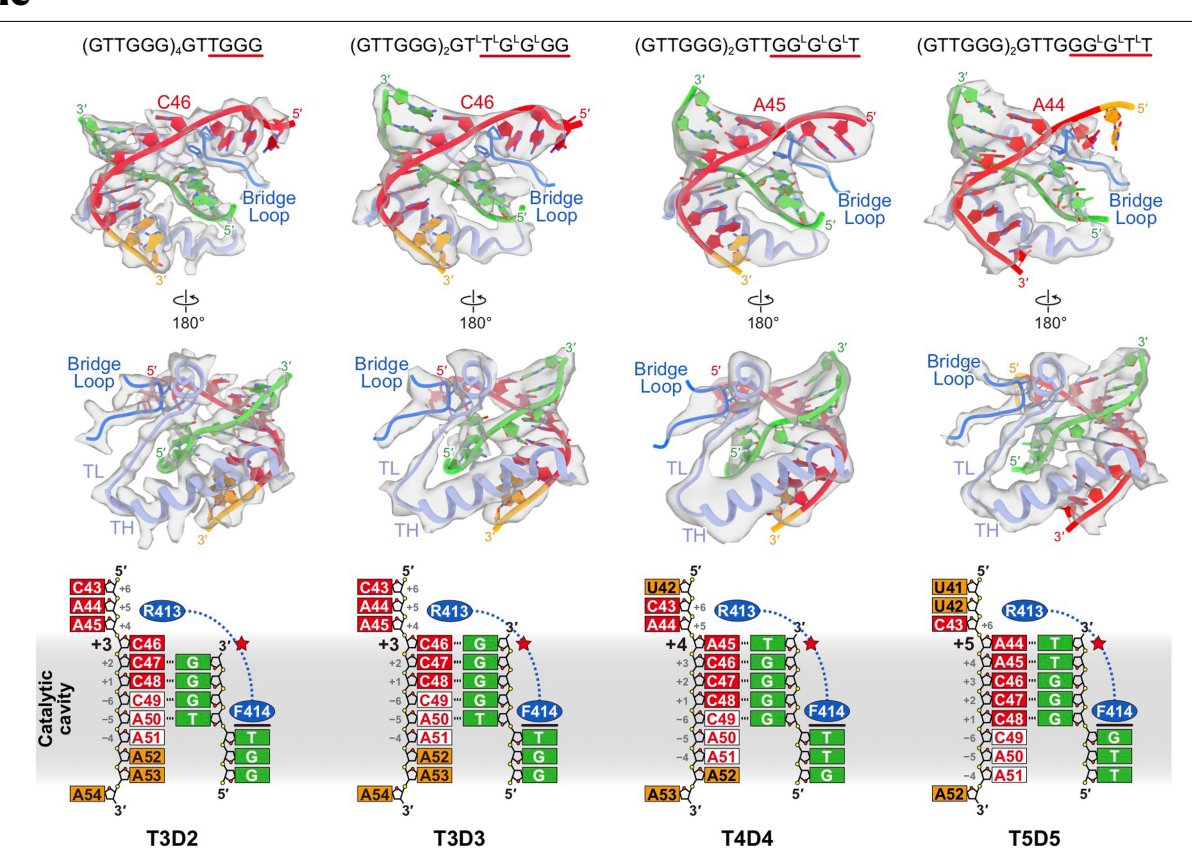
interactions. a–**d**, p50 OB–TERT interactions. **a**, Rainbow-coloured ribbon diagram of p50 OB with secondary structure elements labelled. **b**, Comparison of p50 OB (red) and human TPP1 OB (grey) (PDB 2l46) structures. **c**, TEN loop (amino acids 121–126) passes through a hydrophobic cleft of p50 OB. This loop is a disordered loop in the TEN-domain crystal structure⁷¹. **d**, Structure-based sequence alignment of p50 OB and human TPP1 OB. The secondary structure elements of p50 OB (red) and TPP1 OB (grey) are shown above and below the sequence alignment, respectively. Residues located at the interface between p50 OB and TERT are highlighted in yellow. The NOB and TEL patch residues in human TPP1 OB are indicated and coloured in yellow. The phosphorylation site Ser111 of TPP1 OB is coloured in green. Scaffold residues of $L_{\alpha 2-\beta 4}$ shown in Fig. 2a (bottom) are coloured in blue. **e**–**h**, Teb1C–sstDNA interactions. **e**, Path

of sstDNA from active site to TebIC. Low-pass-filtered cryo-EM density of sstDNA (transparent surface) is superimposed with the unfiltered DNA density (green) to better show its flexible region from $T_{\rm 20}$ to $G_{\rm 22}$. Cryo-EM densities corresponding to TERT domains, TER and TebIC are coloured as in Fig. 1d. \boldsymbol{f} , Sequence of the sstDNA used for the cryo-EM sample preparation with the template and TebIC-interacting regions indicated. Nucleotides from $G_{\rm 1}$ to $G_{\rm 16}$ are invisible in the cryo-EM map. \boldsymbol{g} , Interactions between sstDNA nucleotides and TebIC as indicated in \boldsymbol{e} . Intermolecular hydrogen bonds and stacking interactions are shown as dashed yellow lines and black arrows, respectively. \boldsymbol{h} , Specific interactions between TebIC residues Lys660 and Glu667 and sstDNA nucleotide $G_{\rm 19}$ are shown together with their cryo-EM densities. Hydrogen bonds and their lengths are indicated.



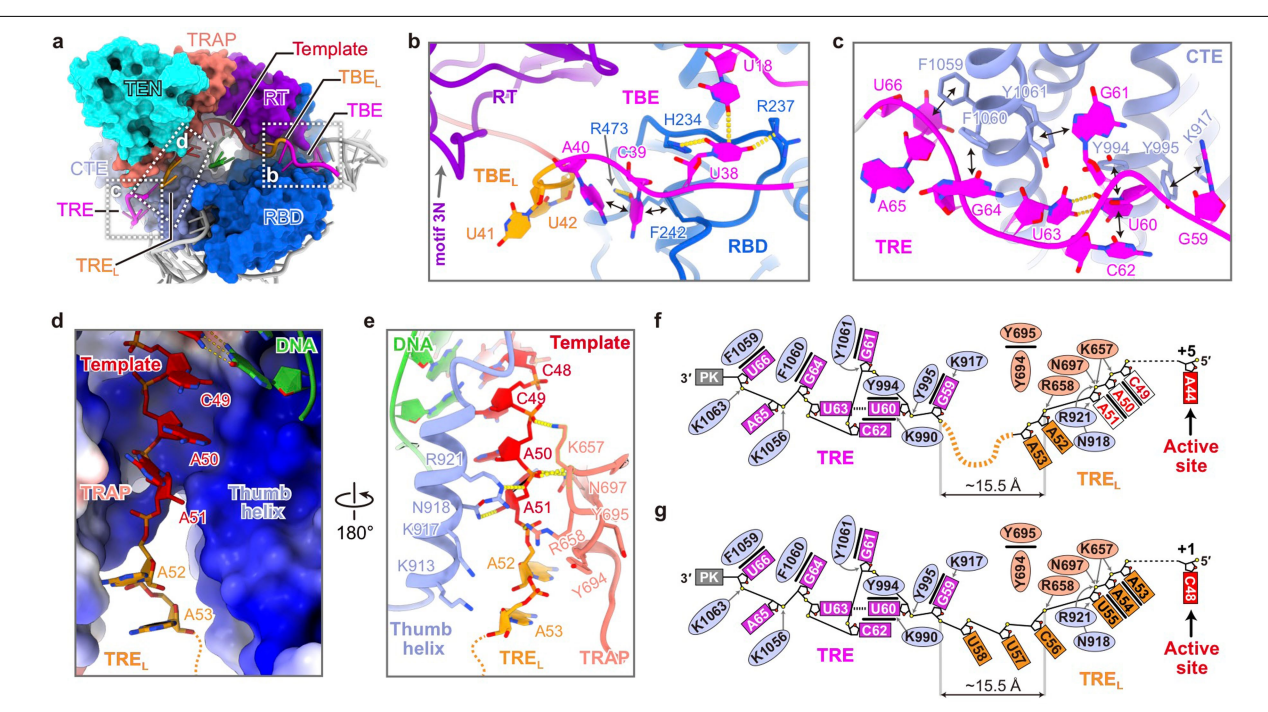
Extended Data Fig. 7 | Cryo-EM reconstructions of telomerase with different sstDNA bound. a, List of sstDNA primers used for cryo-EM sample preparation and their sequences. DNA or LNA nucleotides that pair with the template are underlined. **b**, Resolution of reconstructions determined by gold-standard FSC at the 0.143 criterion. **c**, **d**, Cryo-EM data processing workflow of telomerase T4D4 and T5D5, and evaluations of the final reconstructions. Initial particle screening processes are analogous to those

described in the data processing workflow of telomerase T3D2 (Methods) and are omitted for brevity. Focused 3D classifications were performed to separate DNA-free and DNA-bound particles. Short duplexes were observed in both of T4D4 and T5D5 reconstructions. For telomerase T5D5, there is a subset of particles with a longer duplex that we attribute to the greater stability conferred on the duplex by LNA nucleotides at the thermodynamically most stable duplex (dGGGGT·rACCCC) formed in the previous step.



 $\label{lem:extended} \textbf{Extended Data Fig. 8} \ | \ \textbf{Template-DNA duplexes in telomerase structures at different steps of telomeric DNA synthesis.} \ Top, sequences of sstDNA primers. $T^L \text{ or } G^L \text{ denotes LNA nucleotide.} DNA \text{ or LNA nucleotides that pair with the template are underlined.} Middle, ribbon diagrams of the duplex, template-adjacent nucleotides, bridge loop, TH and TL superimposed with TL superimposed w$

cryo-EM densities (transparent surfaces). Bottom, schematics of the duplexes. The active site (red star), bridge loop residues (Arg413 and Phe414), and catalytic cavity (grey shade) in different structures are aligned to show the relative positions of the duplex. TER and DNA nucleotides are colour-coded as in Fig. 4.



Extended Data Fig. 9 | **Structural details of template boundary determination (TBE, TBE_L, TRE_L and TRE) in telomerase T5D5. a**, Telomerase catalytic cavity in telomerase T5D5 with TER (grey) and DNA (green) shown as ribbon and TERT shown as surface (coloured). TBE, TBE_L, template, TRE_L and TRE nucleotides are highlighted as indicated. $\mathbf{b}-\mathbf{e}$, Detailed interactions between TERT and TER in regions as indicated in \mathbf{a} . Intermolecular hydrogen bonds and stacking interactions are shown as dashed yellow lines and black arrows, respectively. The electrostatic surface of the TRAP–TH channel is

shown in \mathbf{d} . \mathbf{f} , Schematic showing specific interactions between TERT and TRE $_L$ TRE as shown in \mathbf{c} , \mathbf{e} . Nucleotides from A_{54} to A_{58} are unmodelled and indicated as dashed orange lines. \mathbf{g} , Predicted TRE and TRE $_L$ conformation when the template is at the +1 position (template nucleotide C_{48} at the active site). TRE $_L$ nucleotides C_{56} , U_{57} and A_{58} would be fully stretched (about 5–6 Å phosphate-to-phosphate distance for each nucleotide) to span the distance from the neck of the TRAP–TH channel to the anchored TRE.

Extended Data Table 1 | Cryo-EM data collection, refinement and validation statistics

	Telomerase T3D2 (EMDB-23437) (PDB 7LMA)	Telomerase T4D4 (EMDB-23438)	Telomerase T5D5 (EMDB-23439) (PDB 7LMB)
Data collection and processing			
Magnification	105,000	105,000	105,000
Voltage (kV)	300	300	300
Electron exposure (e-/Ų)	48	48	48
Defocus range (µm)	-0.84.0	-0.84.0	-0.84.0
Pixel size (Å)	1.36	1.36	1.36
Symmetry imposed	C1	C1	C1
Initial particle images (no.)	3,816,856	1,749,767	3,951,672
Particle images after class2d (no.)	945,254	373,757	764,707
Final particle images (no.)	193,117	28,297	120,360
Map resolution (Å)	3.3	4.4	3.8
FSC threshold	0.143	0.143	0.143
Map resolution range (Å)	3.0 - 6.0	4.4 - 8.0	3.5 - 7.0
Refinement			
Initial model used (PDB code)	6D6V		7LMA
Model resolution (Å)	4.1		4.4
FSC threshold \('	0.5		0.5
Map sharpening B factor (Å ²)	-82.0		-130.8
Model composition			
Non-hydrogen atoms	18,672		18,498
Protein residues	1,837		1,837
RNA/DNA Nucleotides	170		162
Ligands	1		1
R.m.s. deviations			
Bond lengths (Å)	0.004		0.005
Bond angles (°)	0.858		0.915
Validation			
MolProbity score	1.66		2.02
Clashscore	6.61		11.64
Poor rotamers (%)	0.91		0.06
Ramachandran plot			
Favored (%)	95.69		93.31
Allowed (%)	4.31		6.69
Disallowed (%)	0.00		0.00

nature research

Corresponding author(s):	Juli Feigon and Z. Hong Zhou		
Last updated by author(s):	Feb 24, 2021		

Reporting Summary

Nature Research wishes to improve the reproducibility of the work that we publish. This form provides structure for consistency and transparency in reporting. For further information on Nature Research policies, see our Editorial Policies and the Editorial Policy Checklist.

For all statistical analyses, confirm that the following items are present in the figure legend, table legend, main text, or Methods section

_				
C	۱۵.	⊢i.	~+	ics
	1 4	יוו	< I	11 5

	an ocaciocidai an	any sees, comment and the remaining received and procedure in the negative, cause regently, main teach, or interned sections					
n/a	Confirmed						
	\square The exact sample size (n) for each experimental group/condition, given as a discrete number and unit of measurement						
	A stateme	A statement on whether measurements were taken from distinct samples or whether the same sample was measured repeatedly					
\boxtimes	The statistical test(s) used AND whether they are one- or two-sided Only common tests should be described solely by name; describe more complex techniques in the Methods section.						
\boxtimes	A descript	ion of all covariates tested					
\boxtimes	A description of any assumptions or corrections, such as tests of normality and adjustment for multiple comparisons						
	A full description of the statistical parameters including central tendency (e.g. means) or other basic estimates (e.g. regression coefficient) AND variation (e.g. standard deviation) or associated estimates of uncertainty (e.g. confidence intervals)						
\boxtimes	For null hypothesis testing, the test statistic (e.g. <i>F</i> , <i>t</i> , <i>r</i>) with confidence intervals, effect sizes, degrees of freedom and <i>P</i> value noted <i>Give P values as exact values whenever suitable.</i>						
\boxtimes	For Bayesian analysis, information on the choice of priors and Markov chain Monte Carlo settings						
\boxtimes	For hierarchical and complex designs, identification of the appropriate level for tests and full reporting of outcomes						
Estimates of effect sizes (e.g. Cohen's d , Pearson's r), indicating how they were calculated							
Our web collection on <u>statistics for biologists</u> contains articles on many of the points above.							
Software and code							
Poli	cy information a	about <u>availability of computer code</u>					
Da	ata collection	SerialEM3.8					
Da	ata analysis	Gautomatch_v0.53, CTFFIND4, RELION3.0, RELION2.1, UCSF Chimera1.13 and ChimeraX1.0, Resmap1.1.4, MotionCor2, Coot0.8.3, PHENIX1.17.1, QuantityOne4.6 (Bio-Rad)					

Data

Policy information about availability of data

All manuscripts must include a <u>data availability statement</u>. This statement should provide the following information, where applicable:

For manuscripts utilizing custom algorithms or software that are central to the research but not yet described in published literature, software must be made available to editors and reviewers. We strongly encourage code deposition in a community repository (e.g. GitHub). See the Nature Research guidelines for submitting code & software for further information.

- Accession codes, unique identifiers, or web links for publicly available datasets
- A list of figures that have associated raw data
- A description of any restrictions on data availability

Cryo-EM density maps have been deposited in the Electron Microscopy Data Bank (EMDB) under accession numbers 23437 (telomerase T3D2), 23438 (telomerase T4D4) and 23439 (telomerase T5D5). The atomic models have been deposited in the Protein Data Bank (PDB) under accession codes 7LMA (telomerase T3D2) and 7LMB (telomerase T5D5). Atomic model and cryo-EM density map of telomerase T3D3 were retrieved from the PDB (accession code 6d6v) and EMDB (accession code EMD-7821). Other structures used in this study were retrieved from the PDB with accession codes 2l46 for TPP1-OB, 3KYL for Tribolium TERT-like protein and 2M22 for TER SL2. Uncropped version of all the gels are included as Supplementary Information Figure 1.

-· I				· C·			
Fiel	C	l-sp	ec	ITIC	rep	or	ting

	ne below that is the best fit for your research. If you are not sure, read the appropriate sections before making your selection.
Life sciences	Behavioural & social sciences Ecological, evolutionary & environmental sciences
For a reference copy of	the document with all sections, see nature.com/documents/nr-reporting-summary-flat.pdf
Lite scier	nces study design
All studies must dis	sclose on these points even when the disclosure is negative.
Sample size	3D reconstructions were calculated from 13,097 images (3.8 million particles) for telomerase T3D2, 5,020 images (1.7 million particles) for telomerase T4D4, and 12,922 images (3.9 million particles) for telomerase T5D5 collected in separate imaging sessions. These are typical image sizes used to obtain high resolution cryo-EM structures.
Data exclusions	For cryo-EM analysis, particles that do not belong to the class of interest or have poor qualities based on well established cryo-EM principle were excluded after rounds of 2D and 3D classification. This is standard practice required to obtain high resolution cryo-EM structure of the class of interest.
Replication	Cryo-EM datasets were collected with multiple samples in separate imaging sessions, yielding consistent results (see Methods section for details). All biochemical experiments, including sample purification and activity assays, were repeated three times and are all reproducible, as indicated in captions of Fig. 1j, 3g, 4h and Extended Data Fig. 1a, 1b, 4d-g.
Randomization	No grouping required for our studies.
Blinding	Blinding was not necessary for structure determination by single-particle cryo-EM method. Since there is no grouping in telomerase activity assay, there is no blinding with respect to grouping.

Reporting for specific materials, systems and methods

We require information from authors about some types of materials, experimental systems and methods used in many studies. Here, indicate whether each material, system or method listed is relevant to your study. If you are not sure if a list item applies to your research, read the appropriate section before selecting a response.

Materials & experimental systems		Methods		
n/a	Involved in the study	n/a	Involved in the study	
\boxtimes	Antibodies	\boxtimes	ChIP-seq	
\boxtimes	Eukaryotic cell lines	\boxtimes	Flow cytometry	
\boxtimes	Palaeontology and archaeology	\boxtimes	MRI-based neuroimaging	
\boxtimes	Animals and other organisms			
\boxtimes	Human research participants			
\boxtimes	Clinical data			
\boxtimes	Dual use research of concern			